

JPRS-CST-92-023  
19 November 1992



# ***JPRS Report***

DISTRIBUTION STATEMENT A  
Approved for public release;  
Distribution Unlimited

# **Science & Technology**

***China  
Stealth/Counter-Stealth Research***

19980601 107

DTIC QUALITY INSPECTED 2

REPRODUCED BY  
U.S. DEPARTMENT OF COMMERCE  
NATIONAL TECHNICAL INFORMATION SERVICE  
SPRINGFIELD, VA 22161

**Science & Technology**  
**China**  
**Stealth/Counter-Stealth Research**

JPRS-CST-92-023

**CONTENTS**

19 November 1992

|  |    |
|--|----|
| Hexagonal Ferrite Ku-Band Radar Absorbent Materials<br>[Guo Bijun, Deng Longjiang, et al.; DIANZI KEJI DAXUE XUEBAO, No 3, Jun 92] ..... | 1  |
| Analysis of Multilayer Frequency-Selective Surfaces<br>[Shen Zhongxiang, Hua Rongxi; DIANZI XUEBAO, Jun 92] .....                        | 4  |
| Motion Compensation Method in ISAR Imaging<br>[Bao Zheng, Deng Wenbiao, et al.; DIANZI XUEBAO, Jun 92] .....                             | 6  |
| Motion Compensation in ISAR Imaging for Isolated Scatter<br>[Meng Jing, Zhang Zhizhong; DIANZI XUEBAO, Jun 92] .....                     | 11 |
| Approach to Superresolution Range-Doppler Imaging<br>[Zhu Zhaoda, Ye Zhenru, et al.; DIANZI XUEBAO, Jul 92] .....                        | 14 |
| Microwave Imaging of Targets Rotating in Small Azimuth Angle Range<br>[Huang Peikang, Xu Xiaojian, et al.; DIANZI XUEBAO, Jun 92] .....  | 19 |
| RCS Analysis of Slot-Array Antennas [Deng Shuhui, Ruan Yingzheng; DIANZI XUEBAO, Jun 92] .....   | 24 |
| Study of Backscattering of Electromagnetic Missiles<br>[Wen Geyi, Ruan Chengli, et al.; DIANZI XUEBAO, Jun 92] .....                     | 26 |

### Hexagonal Ferrite Ku-Band Radar Absorbent Materials

92FE0848A Chengdu DIANZI KEJI DAXUE XUEBAO [JOURNAL OF UNIVERSITY OF ELECTRONIC SCIENCE AND TECHNOLOGY (UEST) OF CHINA] in Chinese Vol 21 No 3, Jun 92 pp 312-316

[Article by Guo Bijun [6665 3880 0689], Deng Longjiang [6772 7893 3068], and Chen Xuanzhen [7115 6693 5271] of the Department of Materials Science and Engineering, UEST, Chengdu 610054: "Hexagonal Ferrite Ku-Band Radar Absorbers"; MS received 8 Sep 91, revised 28 Oct 91; project supported by the Preliminary Research Fund of MMEI]

#### [Text] Abstract

The design concept and preparation technique of hexagonal-ferrite-based Ku-band radar absorbent materials (RAM) is discussed. The physical properties and measured electromagnetic parameters are presented. Finally, preliminary application results are described. The absorbance is greater than 12 dB in the 2-cm band. If the composition of the coating is further adjusted, an absorbance of greater than 10 dB can be achieved in the 2-3 cm band (8-18 GHz) range.

Key Words: Ku-band, ferrite, absorber, spontaneous resonance, radar absorber, coprecipitation technique

Classification: TM277

#### I. Introduction

The use of magnetic materials to absorb microwave energy is based on spontaneous resonance. When the microwave frequency coincides with the natural resonance frequency of the material, maximum absorption occurs. The spontaneous resonance frequency is proportional to the anisotropic magnetic field inside the material. Hexagonal ferrites have a high anisotropic field. Therefore, their natural resonance frequencies are high and can be used to absorb microwave energy. Elements such as Co and Ti are used to replace the  $Fe^{+++}$  ion in  $BaFeO_{19}$  to produce a microwave absorber  $Ba(CoTi)_xFe_{12-x}O_{19}$  by ion substitution. The anisotropic field can vary over a wide range as a function of  $x$ .

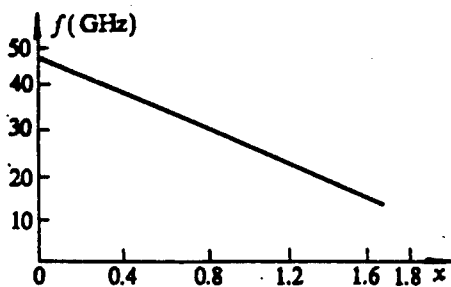


Figure 1.  $Ba(CoTi)_xFe_{12-x}O_{19}$  Natural Resonance Frequency vs.  $x$

Consequently, it is possible to produce a wide-band microwave absorber. Figure 1 shows how the natural frequency of  $Ba(CoTi)_xFe_{12-x}O_{19}$  decreases as a function of  $x$ .

In addition to composition, the shape, size and orientation of the absorbent power have significant effects on its absorption characteristics. When the power size is reduced to the monodomain level, the domain-wall resonance mechanism no longer exists. At this time, the natural resonance frequency of the power increases slightly. However, the maximum microwave energy it is capable of absorbing falls slightly as well, as shown in Figure 2. The powder prepared in this work is approximately 7-10  $\mu m$  in size.

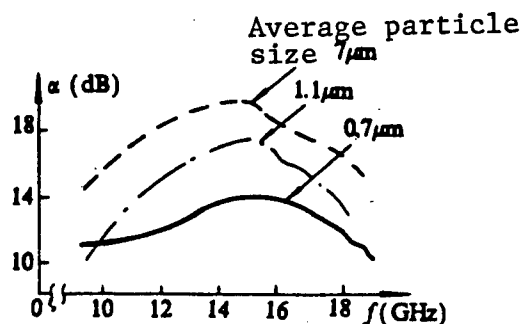


Figure 2. Effect of Powder Size on Microwave Absorbance  $\alpha$

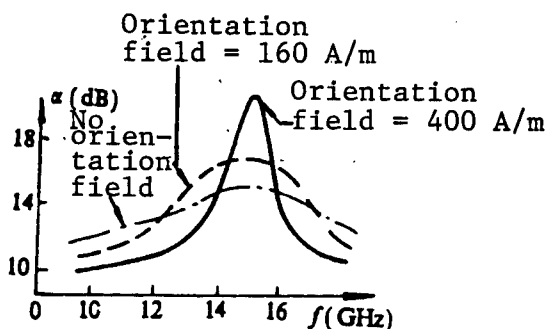


Figure 3. Effect of Magnetic Field Orientation on Microwave Absorbance  $\alpha$

#### II. Experimental Results

High-purity  $BaCO_3$ ,  $Fe_2O_3$ ,  $CoO$  and  $TiO_2$  are used as raw materials. They are weighed stoichiometrically and then ground in a ball mill for 8 hours. The powder is pre-heated at 1280-1350°C, crushed and then sintered. After it is crushed again and sieved, it finally goes through an annealing process. The physical properties and electromagnetic parameters of different M-phase powders of different  $x$  content were experimentally determined. The results are as follows:

1) A scanning electron micrograph of the powder, shown in Figure 4, clearly proves that the powder is hexagonal and the average particle size is  $a < 10 \mu\text{m}$ .



Figure 4. Scanning Electron Micrograph of a Hexagonal Ferrite Ku-Band Radar Absorber

2) The X-ray diffraction analysis result, shown in Figure 5, indicates that the material is a single M-phase material.

3) The specific saturated magnetization moment  $\sigma_s$  is measured using a magnetic balance and  $\sigma_s = 54.0$  (emu/g).

4) An HP8510B network analyzer was used to determine electromagnetic parameters such as relative complex

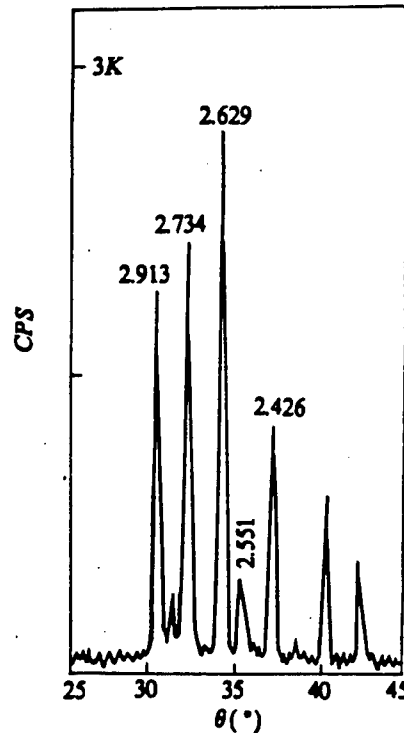


Figure 5. X-Ray Diffraction Pattern of Ferrite Ku-Band Absorber

magnetic permeability  $\mu_r = \mu_r' - j\mu_r''$  and relative complex dielectric permeability  $\epsilon_r = \epsilon_r' - j\epsilon_r''$ . The results are shown in Table 1.

Table 1. Relative Complex Magnetic Permeability and Dielectric Permeability, HP8510B Network Analyzer

| F (GHz) | $E_r'$ | $E_r''$ | $E_r''/E_r'$ | $U_r'$ | $U_r''$ | $U_r''/U_r'$ |
|---------|--------|---------|--------------|--------|---------|--------------|
| 12.40   | 6.955  | 0.076   | 0.011        | 1.796  | 0.323   | 0.100        |
| 13.50   | 7.032  | 0.079   | 0.011        | 1.784  | 0.727   | 0.407        |
| 14.50   | 7.036  | 0.121   | 0.017        | 1.360  | 0.998   | 0.729        |
| 15.50   | 7.031  | 0.100   | 0.015        | 1.001  | 0.830   | 0.820        |
| 16.50   | 7.021  | 0.119   | 0.017        | 0.924  | 0.616   | 0.667        |
| 17.50   | 7.021  | 0.119   | 0.017        | 0.954  | 0.520   | 0.546        |
| 18.00   | 7.078  | 0.061   | 0.007        | 0.956  | 0.516   | 0.540        |

### III. Application

1) The initial Ku-band RAM made have no other additives besides an epoxy binder. Table 2 shows the reflective characteristics of the coated specimens.

Table 2. Reflective Characteristics of RAM Made of Ferrites and Epoxy Binder (absorber thickness 1.5 mm, area 180 x 180 mm<sup>2</sup>, single layer, backed by metal plate)

| Frequency (GHz) | Reflectivity (dB) | Frequency (GHz) | Reflectivity (dB) |
|-----------------|-------------------|-----------------|-------------------|
| 12.40           | -3.22             | 15.40           | -9.38             |
| 12.60           | -3.86             | 15.60           | -9.14             |
| 12.80           | -4.62             | 15.00           | -8.62             |

**Table 2. Reflective Characteristics of RAM Made of Ferrites and Epoxy Binder  
(absorber thickness 1.5 mm, area 180 x 180 mm<sup>2</sup>, single layer, backed by metal plate) (Continued)**

| Frequency (GHz) | Reflectivity (dB) | Frequency (GHz) | Reflectivity (dB) |
|-----------------|-------------------|-----------------|-------------------|
| 13.00           | -6.24             | 16.00           | -8.06             |
| 13.20           | -6.98             | 16.20           | -8.48             |
| 13.40           | -7.68             | 16.40           | -8.74             |
| 13.60           | -8.58             | 16.60           | -8.90             |
| 13.80           | -9.72             | 16.80           | -9.34             |
| 14.00           | -10.50            | 17.00           | -9.52             |
| 14.20           | -10.74            | 17.20           | -9.90             |
| 14.40           | -10.88            | 17.40           | -10.06            |
| 14.60           | -10.78            | 17.60           | -9.86             |
| 14.80           | -10.26            | 17.80           | -10.54            |
| 15.00           | -9.90             | 18.00           | -4.04             |
| 15.20           | -9.86             |                 |                   |

2) The reflective characteristics of specimens coated with a combination of ferrite and other absorbers are shown in Tables 3 and 4.

**Table 3. Reflective Characteristics of Microwave RAM Made of Ferrite and Other Absorbers  
(absorber thickness 1.29 mm, area 180 x 180 mm<sup>2</sup>, single layer, backed with metal plate)**

| Frequency (GHz) | Reflectivity (dB) | Frequency (GHz) | Reflectivity (dB) |
|-----------------|-------------------|-----------------|-------------------|
| 12.40           | -10.20            | 15.40           | -20.42            |
| 12.60           | -11.40            | 15.60           | -22.52            |
| 12.80           | -12.70            | 15.80           | -22.26            |
| 13.00           | -15.60            | 16.00           | -24.92            |
| 13.20           | -17.02            | 16.20           | -24.54            |
| 13.40           | -20.60            | 16.40           | -24.66            |
| 13.60           | -24.82            | 16.60           | -24.42            |
| 13.80           | -26.28            | 16.80           | -22.88            |
| 14.00           | -24.50            | 17.00           | -21.82            |
| 14.20           | -22.78            | 17.20           | -19.52            |
| 14.40           | -21.02            | 17.40           | -17.64            |
| 14.60           | -20.54            | 17.60           | -16.10            |
| 14.80           | -19.62            | 17.80           | -14.50            |
| 15.00           | -20.38            | 18.00           | -10.78            |
| 15.20           | -20.86            |                 |                   |

**Table 4. Reflective Characteristics of Microwave RAM Coated With Ferrites and Other Thickening Agents  
(absorber thickness 1.26 mm, area 180 x 180 mm<sup>2</sup>, single layer, backed with metal plate)**

| Frequency (GHz) | Reflectivity (dB) | Frequency (GHz) | Reflectivity (dB) |
|-----------------|-------------------|-----------------|-------------------|
| 12.40           | -12.06            | 15.40           | -19.58            |
| 12.60           | -12.98            | 15.60           | -20.56            |
| 12.80           | -13.80            | 15.80           | -19.52            |
| 13.00           | -15.68            | 16.00           | -20.66            |
| 13.20           | -16.94            | 16.20           | -20.42            |
| 13.40           | -17.90            | 16.40           | -20.40            |

**Table 4. Reflective Characteristics of Microwave RAM Coated With Ferrites and Other Thickening Agents (absorber thickness 1.26 mm, area 180 x 180 mm<sup>2</sup>, single layer, backed with metal plate) (Continued)**

| Frequency (GHz) | Reflectivity (dB) | Frequency (GHz) | Reflectivity (dB) |
|-----------------|-------------------|-----------------|-------------------|
| 13.60           | -19.12            | 16.60           | -20.30            |
| 13.80           | -19.72            | 16.80           | -18.98            |
| 14.00           | -19.20            | 17.00           | -18.82            |
| 14.20           | -19.34            | 17.20           | -17.32            |
| 14.40           | -18.56            | 17.40           | -16.06            |
| 14.60           | -18.94            | 17.60           | -15.32            |
| 14.80           | -18.82            | 17.80           | -14.34            |
| 15.00           | -19.58            | 18.00           | -12.52            |
| 15.20           | -20.14            |                 |                   |

3) Coated specimens weigh approximately 3.52 kg/m<sup>2</sup>.

From the reflective characteristics of the two types of coatings shown above, we can see that:

1) The absorbance of the specimen can reach above 12 dB over the entire 2-cm band. This indicates that such absorbers can cover the entire Ku band.

2) If the absorbent coating formula and electric structure can be further adjusted, it is highly probable that a wide-bandwidth, high-absorbance coating which covers the 2-3 cm (8-18 GHz) band with an absorbance of more than 10 dB can be made.

3) Compared to conventional ferrite-based RAM, the Ku-band coating developed is thicker, but lighter in weight. This is especially critical for an aircraft.

#### IV. Conclusions

Using ion substitution, it is possible to control the microwave operating frequency by replacing some of the Fe<sup>+++</sup> in BaFe<sub>12</sub>O<sub>19</sub>. The new hexagonal ferrite developed is an excellent Ku-band absorber. The successful development of such a RAM is of significant importance to the preparation of wide-band stealth materials.

#### References

1. Amin, M. B., James, J. R., "Techniques for Utilization of Hexagonal Ferrites in Radar Absorbers," *THE RADIO AND ELECTRONIC ENGINEER*, 1981, 51 (5): 209-218.
2. Yoshiyuki Naito, Kunihiro Suetake, "Application of Ferrite to Electromagnetic Wave Absorber and Its Characteristics," *IEEE TRANS. ON MICROWAVE THEORY TECH.*, 1971, MTT-19: 65-72.
3. Nedkov, I., Detkov, A., Karpov, V., "Microwave Absorption in Sc-Substituted Ba Hexaferrite Powders," *IEEE TRANS. ON MAG*, 1990, 26 (5): 1483-1484.

#### Analysis of Multilayer Frequency-Selective Surfaces

92FE0801F Beijing DIANZI XUEBAO  
[ACTA ELECTRONICA SINICA] in Chinese  
Vol 20 No 6, Jun 92 pp 85-88

[Article by Shen Zhongxiang [3088 1813 4382] and Hua Rongxi [5478 2837 0823] of Nanjing Institute of Aeronautics: "Analysis of Multilayer Frequency-Selective Surfaces"; MS received Nov 90, revised Aug 91]

#### [Excerpts] Abstract

The scattering characteristics of multilayer frequency-selective surfaces (FSS) are analyzed by the method of moments in conjunction with generalized scattering matrix theory. Through the introduction of a generalized waveguide, a unified treatment of a multilayer FSS with an arbitrarily shaped element is realized. As examples, the scattering characteristics of several FSS structures are computed. The results are in good agreement with published experimental data.

Key Words: electromagnetic wave, scattering, frequency-selective surface.

#### I. Introduction

It is well known that a FSS has the property of a bandpass or band-rejection filter. It is widely used in radomes, reflector antennas and beam-control systems. A great deal of work has been done on the analysis of single-layer FSSs. Many methods have been presented, including mode matching,<sup>1,3</sup> spectral domain<sup>5</sup> and subdomain moment.<sup>6</sup> However, these methods are universal and have their limitations. As for the analysis of multilayer FSSs, it is limited to two layers.<sup>7,8</sup>

In this work, the scattering characteristics of a multilayer FSS are analyzed using the method of moments and generalized scattering matrix theory. The basic idea is to introduce the generalized waveguide concept and consider each element on the FSS as a joint for two generalized waveguides. The intrinsic mode of a generalized waveguide is the periodic Floquet mode.<sup>12</sup> The method of moments is used to find the generalized scattering matrix at the waveguide joint. Then, the scattering parameters of the multilayer FSS can be calculated based on the generalized scattering matrix.

II. Theoretical Analysis

The following is an analysis of the theory using an infinite conductor screen with a periodic two-dimensional array of holes. For a two-dimensional planar bonded-plate array, the analysis can be derived from the results of this work on the basis of duality. The structure studied is shown in Figure 1, where  $d_1$  and  $d_2$  are the periods along the x-axis and s-axis, respectively, and  $\alpha$  is the angle between the two axes. [passage omitted]

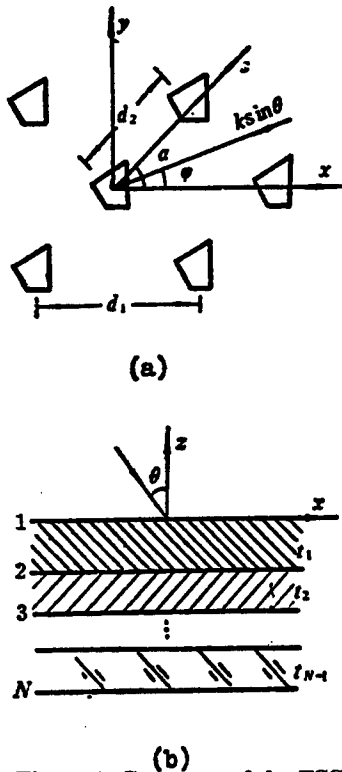


Figure 1. Geometry of the FSS

III. Numerical Results

The theory discussed above is used to calculate the reflection and transport characteristics of a plane wave incident upon a single- and a double-layer FSS. Specifically, the FSS scattering characteristics of infinite plates with an array of rectangular and circular holes are calculated in this work. In the computation,  $W_q = M_q$ . Furthermore, in order to be universally applicable, the intrinsic mode of the cross section of the waveguide, in the shape of the hole on the plate, is chosen to express  $M_q$ . In the actual computation,  $Q = 10$ , i.e., one considers the lowest 10 modes in the waveguides. In equation (1), p and q should be selected so that  $t_{pq} < 11/k$  (where k is the wave number in free space). Figures 3 and 4 show the reflection and transmission characteristics of a vertically incident TE wave on a single-layer FSS. The transmission frequency characteristics of a vertically incident TE wave on a double-layer FSS (comprised of

rectangular arrays) are shown in Figure 5. Other results in existing literature are also shown in the figures. It is obvious that they are in excellent agreement.

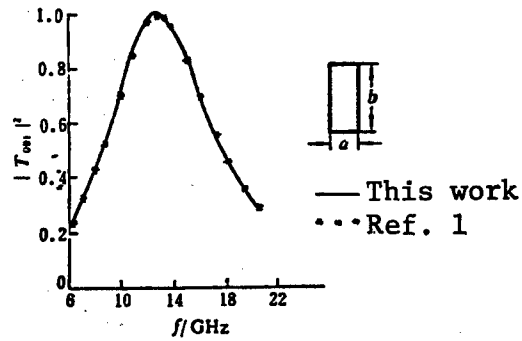


Figure 3. Transmission Characteristics of Main Mode on Infinite Plate With Two-Dimensional Rectangular Array ( $d_1 = 7.6$  mm,  $d_2 = 15.2$  mm,  $\alpha = 90^\circ$ ,  $a = 1.27$  mm,  $b = 13.5$  mm,  $\epsilon_{\gamma 1} = \epsilon_{\gamma 2} = 1$ )

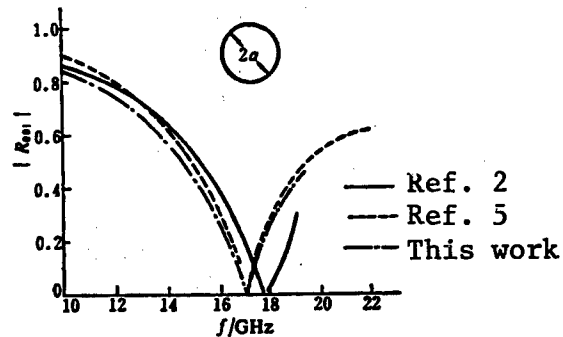


Figure 4. Reflective Index of Main Mode From Single-Layer Circular Array ( $d_1 = d_2 = 17.3$  mm,  $a = 6$  mm,  $\alpha = 60^\circ$ ,  $\epsilon_{\gamma 1} = \epsilon_{\gamma 2} = 1$ )

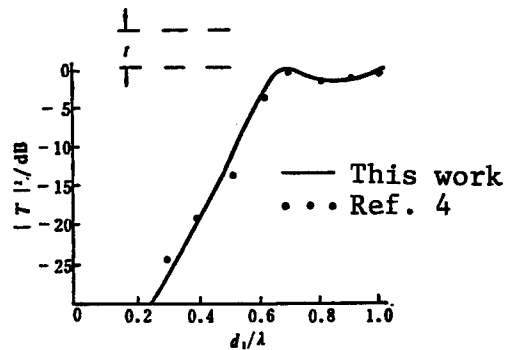


Figure 5. Power Transmission of Double-Layer Rectangular Array FSS ( $d_1 = d_2$ ,  $\alpha = 90^\circ$ ,  $a = b = 0.7 d_1$ ,  $t = 0.5a$ ,  $\epsilon_{\gamma 1} = \epsilon_{\gamma 2} = \epsilon_{\gamma 3} = 1$ )

#### IV. Conclusions

The scattering characteristics of multilayer frequency-selective surfaces (FSS) are analyzed by the method of moments in conjunction with generalized scattering matrix theory. The theory can be applied to any multilayer FSS structure with any shape of elements. The analysis done in this work is based on the assumption that the thickness of the FSS is infinitely thin. Nevertheless, it can be easily extended to multilayer FSSs with a finite thickness.

#### References

1. C. C. Chen, IEEE TRANS., 1970, AP-18 (9): 660-665.
2. C. C. Chen, IDDD TRANS., 1971, MTT-19 (5): 475-483.
3. J. P. Montgomery, IEEE TRANS., 1975, AP-23 (1): 70-75.
4. S. W. Lee, et al.; IEEE TRANS., 1982, AP-30 (9): 904-909.
5. R. Mittra, et al., IEEE TRANS., 1984, AP-32 (5): 533-536.
6. C. H. Chan, et al., IEEE TRANS., 1990, AP-38 (1): 40-50.
7. F. S. Johansson, IEE PROC., 1985, 132 (5): 319-325.
8. J. C. Vardaxoglou, E. A. Parker, INTER. J. ELECTRONICS, 1985, 58 (5): 827-830.
9. R. C. Hall, et al., IEEE TRANS., 1988, AP-36 (4): 511-517.
10. K. J. Webb, R. Mittra, IEEE TRANS., 1985, MTT-33 (10): 1004-1010.
11. R. F. Harrington, "Time-Harmonic Electromagnetic Fields," New York: McGraw-Hill, 1961.
12. N. Amitay and V. Galindo, BELL SYST. TECH. J., 1968, 47 (11): 1903-1932.
13. K. C. Gupta, et al., "Computer-Aided Design of Microwave Circuits," Dedham, MA: Artech House, 1981.

#### Shen Zhongxiang

Born in July 1966 in Haiyan, Zhejiang, he graduated from the University of Electronic Science and Technology in 1987. In 1990, he received his Master's degree in Radio and Electrical Engineering from Southeast University. Since April 1990, he has been teaching in the Department of Electronic Engineering at Nanjing Aeronautical Institute.

#### Hua Rongxi

Born in Jiangsu in 1936, he graduated from the Department of Radio at Beijing Institute of Technology in

1960. He is an Associate Professor in the Department of Electronic Engineering at Nanjing Aeronautical Institute. His research interests include antenna arrays, microstrip antennas, microwave devices and electromagnetic scattering.

#### Motion Compensation Method in ISAR Imaging

92FE0801A Beijing DIANZI XUEBAO  
[ACTA ELECTRONICA SINICA] in Chinese  
Vol 20 No 6, Jun 92 pp 1-6

[Article by Bao Zheng [0202 6927], Deng Wenbiao [6772 2429 1753], and Yang Jun [2799 6511] of Xidian University, Xian, 710071: "Motion Compensation Method in ISAR Imaging"; MS received May 90, revised Mar 91]

#### [Text] Abstract

Motion compensation is a key problem in ISAR (inverse synthetic aperture radar). Usually, compensation is made using an isolated point on the target. In reality, this isolated point may not exist. This paper presents a new scheme to compensate for the echo of a continuous target.

Key Words: inverse synthetic aperture radar, radar imaging, motion compensation.

#### I. Introduction

ISAR imaging belongs to small-rotation-angle observation imaging with a rotation angle ranging from 3°-5°. It is known<sup>1</sup> that targets such as airplanes, missiles and ships are considered as a series of discrete scattering points (perhaps very concentrated) as far as a high-resolution radar is concerned. Within an azimuth angle of less than 30°, these scattering points can be considered approximately fixed and the scattering strength is a constant. Hence, ISAR imaging is used to plot the distribution of these scattering points. If the target is on a rotating platform, this is not difficult to accomplish. Therefore, that case will not be discussed.

A real moving target, as far as a radar is concerned, has a translational component in addition to rotation that contributes to imaging. Hence, it is necessary to select a reference point on the target prior to ISAR imaging in order to compensate for the translational component of the reference point. This is equivalent to placing the reference point on the rotation axis. The imaging process is carried out based on compensated data.

ISAR imaging can handle a variety of signals. In this paper, the discussion is limited to narrow pulses. The results can be extended to other types of signals.

#### II. Concept and Purpose of Compensation

In ISAR imaging, there is relative motion between target and radar. As shown in Figure 1, using the target as the reference, i.e., choosing a point on the target as a still reference point, the radar moves along the broken line (with dashes and dots) shown in the sketch. As far as

rotating platform imaging is concerned, the radar should be in circular motion along the arc shown in the sketch. Therefore, the purpose of motion compensation is to provide proper adjustment to the time delay of the echo. (Intensity should also be adjusted. However, if relative distance does not vary much, intensity variation can be neglected.)

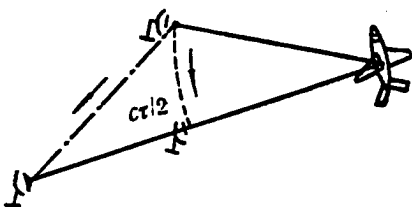


Figure 1. Relative Motion Between Radar and Target

Assume an echo is expressed as follows:

$$s(t) = f(t) \exp(j\omega_0 t) \quad (1)$$

where  $f(t)$  is the complex envelope of the echo and  $\omega_0$  is the angular frequency of the carrier.

By delaying the echo by a time interval  $\tau$ , the delayed signal is:

$$s(t-\tau) = f(t-\tau) \exp(-j\omega_0 \tau) \exp(j\omega_0 t) \quad (2)$$

Usually, radar signals are processed at the fundamental frequency after mixing. After multiplying the above equation by  $\exp(-j\omega_0 t)$ , we obtain the delayed complex envelope  $f(t-\tau) \exp(-j\omega_0 \tau)$ . When the time delay  $\tau$  is changed, the complex envelope  $f(t-\tau)$  and initial phase factor  $\exp(-j\omega_0 \tau)$  will also change. However, the rate of change is different. For an X-band radar, a delay of the order of a millimeter causes significant change in its initial phase. On the other hand, it almost has no effect on the complex envelope when the pulse width is several dozen centimeters. Based on this reason, and the fact that initial phase changes come around every  $2\pi$ , motion compensation can be performed in two steps. The first step is to carry out time delay translational correction (rough compensation). The accuracy is of the order of a centimeter. The next step is to further adjust the initial phase of the corrected echo (fine compensation). The error should be far less than  $\pi/2$ . Upon completion of these two steps, the initial phase is essentially accurate. However, the complex envelope delay might have an error of the order of a centimeter. This should not have any significant effect on imaging.

Hence, if the target has an echo from an apparent isolated scattering point, motion compensation is not difficult. It can be done by simply choosing that isolated point as a reference point to align the envelope and to change the initial phase so that the phased difference across a cycle is zero (which is equivalent to the axis of

rotation). However, only a few special cases have isolated scattering points. Many targets have continuous echoes that are a superposition of echoes from numerous scattering points.

In the event that there is no isolated point, a point from which its delay and phase shift can be determined should be chosen as the reference point. In the following, we shall prove that it is feasible to use the "scattering center of gravity" as a reference point.

### III. Calculation of Time Delay and Phase Shift of Scattering Center of Gravity

The longitudinal and transverse coordinates of the scattering center of gravity of a group of scattering points can be calculated based on their positions and echo intensities. In reality, only echo data is available. The problem is how to calculate the coordinates from echo data alone.

In order to demonstrate how the longitudinal time delay of the scattering center of gravity can be calculated from echo data, let us use the case shown in Figure 2 as an example. In that case, the echoes do not overlap on the time axis. In the  $k$ th observation, if the echo intensity and time delay of each scattering point is  $\sigma_i$  and  $t_{ik}$  ( $i = 1, 2, \dots$ ), then the longitudinal coordinate  $T_k$  of its scattering center of gravity is

$$T_k = \frac{\sum_i \sigma_i t_{ik}}{\sum_i \sigma_i} \quad (3)$$

### Electromagnetic waves

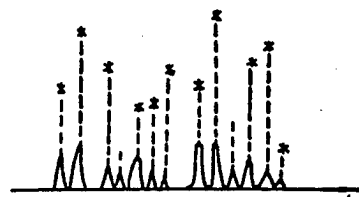


Figure 2. Target Scattering Points and Echoes

However, it is not so simple in real life. The echoes from the scattering points of a continuous target do overlap. In this case, the  $k$ th echo can be expressed as:

$$s_k(t) = \sum_i \sqrt{\sigma_i} v(t - t_{ik}) \quad (4)$$

where  $v(t)$  is the transmitted signal. The complex envelope of the echo is

$$f_k(t) = \sum_i \sqrt{\sigma_i} a(t - t_{ik}) \exp(-j\omega_0 t_{ik}) \quad (5)$$

where  $a(t)$  is the complex envelope of  $v(t)$ . It is obvious that

$$|f_k(t)|^2 = f_k(t) f_k^*(t) = \sum_i \sigma_i |a(t - t_{ik})|^2 + \sum_{i \neq j} \sum_i \sqrt{\sigma_i \sigma_j} a(t - t_{ik}) \cdot a^*(t - t_{jk}) \exp(-j\theta_{ijk}) \quad (6)$$

where  $\theta_{ijk} = \theta_{ik} - \theta_{jk} = \omega_0(t_{ik} - t_{jk})$

The first term in equation (6) is the power of each scattering point. The second term represents the cross term. In practice, it is only necessary to consider the overlapping part of the echoes. As mentioned earlier,  $t_{ik}$  varies only slightly for neighboring echoes and has no effect on  $a(t)$ . However, phase may vary considerably in a random fashion. In an approximation,  $\theta_{ijk}$  can be treated as a symmetrically and randomly distributed variable with a zero mean value for each observation. Hence, when taking the statistical average of (6), the cross term is zero, i.e.,

$$E[|f_k(t)|^2] = \sum_i \sigma_i |a(t - t_{ik})|^2 \quad (7)$$

This suggests that there is no difference in the calculation of echo power compared to the case where all the echoes do not overlap from the standpoint of statistical average. Nevertheless, in order to calculate the scattering center of gravity (as shown in equation 3), it is necessary to use

$$\sum_i \sigma_i t_{ik}$$

The echoes from the target can be divided into range rings according to different side lobes. There might be many scattering points inside a range ring (with a specific  $t_{ik}$  value). During continuous observation, due to phase variation, the echo also fluctuates. However, as a statistical average, it is identical to the situation in which every range ring has a single scattering point. In other words, when calculating the time delay of the longitudinal coordinate of the scattering center of gravity with equation (3) based on the echoes obtained, it also fluctuates. However, its average is the correct value.

As a verification, we designed a moving target with 20 scattering points. Figure 3 shows the time delay of the scattering center of gravity calculated from simulated echoes. The disturbance is apparent. After smoothing, it is very close to the original design curve. We also added

some noise to the simulated echoes. The effect of noise amplifies the disturbance, which can be reduced by smoothing.

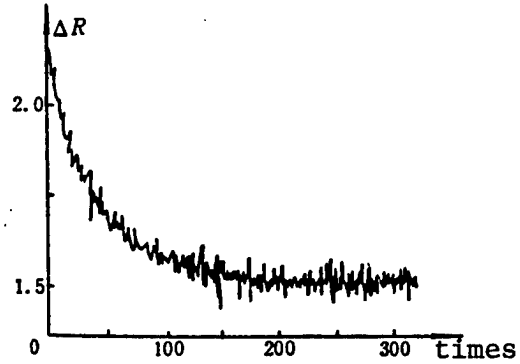


Figure 3. Translational Trajectory of Scattering Center of Gravity

After delay compensation of the complex envelope, the next step is initial phase compensation. The motion of a target can be divided into translational and rotational. The periodic phase shift of the echo from each scattering point is the sum of the phase shifts produced by these two types of motion. The translational phase shift is the same for every scattering point, while the rotational phase shift might be different from point to point. With respect to the rotation axis (reference point), rotational phase shift is zero. Therefore, when the scattering center of gravity is chosen as the reference point, the phase shift at the center of gravity (not necessarily a scattering point) should be calculated and used for initial phase compensation.

If rotation alone is taken into consideration and a stationary reference point is chosen as the origin, then the longitudinal displacement of scattering point  $i$ ,  $\Delta y_i$ , generated as a result of rotation by an angle  $\Delta\phi$  is (see Figure 4):

$$\Delta y_i = R_i \cos(\phi_i - \Delta\phi) - R_i \cos \phi_i = y_i (\cos \Delta\phi - 1) + x_i \sin \Delta\phi \quad (8)$$

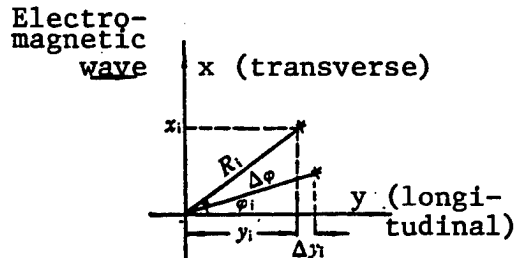


Figure 4. Longitudinal Displacement of Scattering Point Caused by Target Rotation

In reality, the target is several hundred kilometers away and two pulses are separated at most by a few milliseconds; the  $\Delta\phi$  generated by target movement within this time interval is usually less than  $0.01^\circ$ . If  $x_i$  and  $y_i$  are 10 meters, then the first and last terms of equation (8) are of the order of a micron and millimeter, respectively. Hence,

$$\Delta y_i \approx x_i \Delta\phi \quad (9)$$

As far as the  $i$ th echo is concerned, the phase-angle difference between two consecutive observations due to target motion is

$$\Phi_i = (4\pi/\lambda_0) x_i \Delta\phi \quad (10)$$

If the transverse coordinate of each scattering point is  $x_{ij}$  ( $i = 1, 2, \dots$ ), then the transverse scattering center of gravity is

$$x_0 = \frac{\sum_i \sigma_i x_i}{\sum_i \sigma_i} \quad (11)$$

By multiplying  $(4\pi/\lambda_0) \Delta\phi$  to both sides of the equation above, and by taking equation (10) into consideration, it is possible to obtain the phase-angle difference of the transverse scattering center of gravity after the target rotates by an angle of  $\Delta\phi$ .

$$\Phi_0 = \frac{\sum_i \sigma_i \Phi_i}{\sum_i \sigma_i} \quad (12)$$

In reality, the distribution of scattering points is unknown. We need to find  $\Phi_0$  from the waveform observed. If it is simple as in the case shown in Figure 2 where the echoes do not overlap, the phase shift  $\Phi_1$  can be calculated from the phase change of consecutive echoes. Then,  $\Phi_0$  can be obtained from equation (12) based on the intensity of the echo  $\sigma_i$ .

If the scattering center of gravity is chosen as a stationary reference point, then the phase-angle difference between observations,  $\Phi_0$ , should be zero. Using the  $\Phi_0$  obtained from equation (12) as the initial phased compensation should produce the desired result.

In real life, many sub-echoes may overlap at the same time. In this case, the phase changes of these sub-echoes cannot be determined. In order to obtain  $\Phi_0$  from (12), the easiest way is to replace  $\sigma_i$  with echo power at a specific time (usually in an interval of a pulse width) and to use the phase difference of the echo at this time interval between two consecutive observations as  $\Phi_i$ . Does this arrangement make sense? Let us take a look at the case where only the echoes from two scattering points overlap.

As we mentioned several times earlier, in a few neighboring observation periods, as an approximation, the complex envelope can be considered as stationary. This

means that the echo vector from any scattering point at any instance remains unchanged. Only the phase angle changes. Figure 5 shows the situation involving two scattering points in two consecutive observations. In the figure,  $r_1$  and  $r_2$  are the amplitudes of the echoes at those two scattering points at that instance;  $R_1$  and  $R_2$  are the synthetic amplitudes of the two observations. Using the vector of  $r_1$  as a standard, the phase angle varies by  $\Delta\psi$ . The vector angles of the two sub-echoes in the two observations are  $\theta$  and  $\theta + \Delta\theta$ , with  $\theta = \theta_2 - \theta_1$  and  $\Delta\theta = \Delta\theta_2 - \Delta\theta_1$ , where  $\theta_1, \theta_2$  and  $\Delta\theta_1, \Delta\theta_2$  are the phase angles of the sub-echoes and the phase-angle differences in the second observation, respectively. (The variation of  $\theta_1$  is not shown in the figure.) If  $\Delta\theta$  and  $\Delta\psi$  are both small, then geometrically we can determine that

$$R_1 \approx R_2 \approx R \quad (13)$$

$$\Delta\psi = r_2 \Delta\theta \cos(\theta - \psi) / R \quad (14)$$

If  $\sigma_i$  and  $\Phi_i$  in equation (12) are directly replaced by the echo, the contribution to equation (12) at that moment is  $R^2(\Delta\psi + \Delta\theta_1)$ . After substituting it into equation (14) and taking the geometry shown in Figure 5 into account, we have

$$R^2(\Delta\phi + \Delta\theta_1) = (r_2^2 + r_1 r_2 \cos \theta) \Delta\theta + (r_2^2 + r_1^2 + 2r_1 r_2 \cos \theta) \Delta\theta_1 \quad (15)$$

Taking the average of the above equation over  $\theta$ , we get

$$E[R^2(\Delta\phi + \Delta\theta_1)] = r_1^2 \Delta\theta_1 + r_2^2 \Delta\theta_2 \quad (16)$$

This demonstrates that the phase-angle difference of the

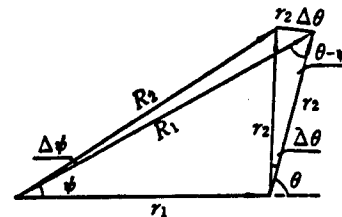


Figure 5. Variation of Echo From a Rotating Target

transverse scattering center of gravity derived from the power and phase difference of the measured waveform is consistent, from the standpoint of statistical average, with that calculated based on all scattering points. Therefore, the phase compensation calculated from the waveform must be filtered to remove disturbance from it.

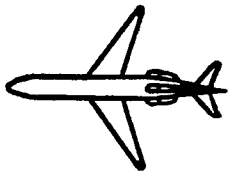
The above is the situation when two sub-echoes overlap. It is easy to extend to more overlapping sub-echoes. In the above discussion, it is also assumed that  $\Delta\theta \rightarrow 0$ . When  $\Delta\theta$  has a finite value, direct analysis is more difficult. Through computer simulation, it was found that there is a difference between the statistical average of the calculated transverse scattering center of gravity and the real value. However, as long as the absolute value of  $\Delta\theta < 0.5$  rad (which covers most cases), the error is less than 5 percent. This kind of error is tolerable in ISAR imaging.

With a repetition frequency of the order of a few milliseconds, the phase-angle differences of various scattering points caused by rotation are small. However, translational motion will cause a larger but equal phase shift at every scattering point. Hence, the phase-angle differences of a scattering point within a period are distributed over a small angular range and this angular range is randomly distributed over  $[0, 2\pi]$ . Since phase angle is a cyclic function of  $2\pi$ , the angular range cannot have any  $2\pi$  jumps when we calculate the phase difference of the scattering center of gravity.

#### IV. Experimental Results

In order to confirm the above analysis, a great deal of simulation and experimental work was done. In computer simulation, a flying scattering point model and an electromagnetic scattering model were employed. Experimentally, measured data from a rotating model was used. Furthermore, simulated flight data was also studied. The results are excellent. Nevertheless, we are most concerned about imaging of flying targets.

We were fortunate to obtain a set of Boeing 727 flight data from Professor Steinberg of the University of Pennsylvania. Figure 6 shows the image generated after motion compensation (aircraft and radar parameters are shown in the figure). Comparing to the actual silhouette of the aircraft at the bottom, it is not difficult to come to the conclusion that the imaging effect is satisfactory. This illustrates that motion compensation based on the scattering center of gravity is a viable approach. This technique will be verified with more experimental data, especially actual moving target data, in the near future.



(a) Sketch of the aircraft



(b) Aircraft image

Figure 6. Imaging Based on Motion Compensated Data

It should be pointed out that the center of mass of the echo and the actual scattering center of gravity coincide

only in a statistical average sense. Hence, it is necessary to smooth out the results while performing complex envelope delay compensation. This technique has proven to be successful in a variety of experimental conditions. As for smoothing of initial phase compensation, computer modeling was also successful. However, it may not work on actual data because there are other factors affecting the initial phase. For instance, instability of emission frequency will cause random disturbance of initial phase and this should not be smoothed out.

Motion compensation in ISAR imaging needs further research. The method of using isolated points as reference points is effective when there are isolated scattering points. However, it becomes useless with targets that have densely distributed scattering points. In this case, the scattering center of gravity method has an edge. Furthermore, the more scattering points there are, the more even the distribution becomes and the more favorable the compensation is. In other words, isolated point and scattering center of gravity complement each other.

#### Acknowledgments

The authors wish to express their gratitude to Professor Steinberg of the University of Pennsylvania for providing the actual flight data, to the ISAR research group at Harbin Institute of Technology for providing microwave darkroom data, and to the 207th Institute of the Ministry of Aerospace Industry for supporting our microwave darkroom experiment.

#### References

1. D. R. Wehher, "High-Resolution Radar," Artech House, 1987.
2. Deng Wenbiao and Bao Zheng, "Relation Between One-Dimensional and Two-Dimensional Imaging of Rotating Targets," XIAN DIANZI KEJI DAXUE XUEBAO [JOURNAL OF XIDIAN UNIVERSITY], Vol 17, No 1, 1990, p 1.
3. Deng Wenbiao, "Basic Characteristics of R-D Imaging of Rotating Targets," DIANZI KEJI DAXUE XUEBAO (Chengdu) [JOURNAL OF UNIVERSITY OF ELECTRONIC SCIENCE AND TECHNOLOGY OF CHINA], Vol 9, No 1, 1990, p 38.
4. C. C. Chen and B. C. Anders, "Target Motion-Induced Radar Imaging," IEEE TRANS., Vol AES-16, No 1, 1980, pp 2-14.
5. M. T. Pickett and C. C. Chen, "Principle of Inverse Synthetic Aperture Radar Imaging," EASCON, 1980, pp 340-345.

#### Bao Zheng

Since graduating from Northwest Institute of Telecommunications Engineering (presently Xidian University) in 1953, he has stayed at the institute to do research and teach. Presently, he is a professor in the Graduate School

of Electronic Engineering and an adviser for doctoral candidates. His areas of interest include signal processing and radar systems. Professor Bao is a member of the Chinese Society of Electronics and an editor of DIANZI XUEBAO [ACTA ELECTRONICA SINICA].

#### Deng Wenbiao

Born in February 1961, he graduated from the Department of Information Engineering at Northwest Institute of Telecommunications Engineering in 1982. He earned his Master's in Engineering from the Department of Radio Technology at Chengdu University of Electronic Science and Technology in 1985 and his Ph.D. in Engineering from Xidian University in 1988. He is engaged in research in areas such as radar imaging, image processing, digital circuitry and digital system diagnosis.

#### Yang Jun

Born in 1965, she graduated from the Department of Electronic Engineering of Xidian University in 1987. In 1990, she earned her Master's degree in signals, circuits and systems from Xidian University. Presently, she is working on her Ph.D. degree at the same institution. Her thesis is in the area of ISAR imaging and motion compensation.

#### Motion Compensation in ISAR Imaging for Isolated Scatterer

92FE0801C Beijing DIANZI XUEBAO  
[ACTA ELECTRONICA SINICA] in Chinese  
Vol 20 No 6, Jun 92 pp 21-27

[Article by Meng Jing [1322 7324] and Zhang Zhizhong [1728 4160 0022] of Nanjing Institute of Electronic Technology, Nanjing 210013; "Motion Compensation in ISAR Imaging for Isolated Scatterer"; MS received May 90, revised Feb 91]

#### [Excerpts] Abstract

When there is a relatively isolated and strong scatterer in the target, ISAR [inverse synthetic aperture radar] motion compensation can be transformed into the alignment of each return and the phase compensation of each return. In this work, the return phase is used as an approximation to estimate the return Doppler frequency. In addition, a novel method is presented to eliminate any ambiguities of Doppler frequency. The target trajectory is re-established using the unambiguous Doppler frequency to align the range of each return.

Key Words: ISAR imaging, motion compensation, Doppler frequency ambiguity resolution.

#### I. Introduction

In microwave imaging with a phased array antenna, the antenna must be aimed at the target or target area for focusing. This is to perform phase compensation for each element and then find the coherent sum. SAR (synthetic aperture radar) or ISAR imaging can be treated as

imaging with a large-aperture phased array antenna. Therefore, each return should be compensated. The difference is that because the aperture is extremely large, it is not only necessary to perform phase compensation but also range alignment for each return. The combination is considered as motion compensation in this paper.

In studying ISAR imaging, because it is difficult to accurately measure the trajectory of the target, motion compensation has always been a challenge. In order to solve this problem, many assumptions have been postulated. For instance, the target has an isolated and strong scatterer and this small scatterer can be resolved from the longitudinal range of the wide transmission signal. Furthermore, the scatterer has a small transverse dimension (which is less than the required transverse resolution). Then, the small scatterer can be treated as a relatively isolated source (a point scatterer in an ideal situation). It has been demonstrated in reference 1 by means of statistical analysis of a great deal of experimental data that the probability that such a relatively isolated scatterer exists is 80 percent when the range resolution is  $\delta_R = 1$  m.

For targets such as airplanes, the isolated scatterers might be wing tips, engines and tails. Under the assumption that such an isolated scatterer could be found, many ISAR imaging experiments on real flying targets or airplane models have been reported.<sup>1-4</sup>

Motion compensation in ISAR imaging primarily involves range alignment for every return. A spatial cross-correlation method and frequency-domain method were used for range alignment in reference 2. Both methods involve a great deal of computation. Here, we will introduce a simple and direct method for range alignment by estimating the unambiguous Doppler frequency in order to re-establish the trajectory of the moving target.

Since the radial velocity of the target is not constant, i.e., its Doppler frequency is not invariant, the Doppler frequency estimated based on the returns accumulated over a period  $\Delta t$  in the past cannot accurately reflect the Doppler frequency at the present time. In this work, we use the phase of the target return to estimate the Doppler frequency of the echo and present a new method to eliminate Doppler ambiguities.

The range alignment method is described below.

#### II. Motion Compensation

In the following discussion, let us assume that the operating wavelength of the radar is  $\lambda = 0.05$  m, and the range resolution is  $\delta_R = 1$  m for the 150 MHz wide-band signal emitted by the radar. After taking the computation load and the transverse resolution required, the pulse repetition frequency (prf) chosen is  $F_r = 100$  Hz.

By using a coherent measurement radar, we can obtain data such as the target range  $R'(t)$  and complex target return  $a'(t)$ . If discrete sampling is employed, we get:

Target range  $R'(i)$ , complex target return  $a'(i,j)$  (where  $i = 1, 2, \dots, N$  represents the  $i$ th transmission (or reception),  $j = 1, 2, \dots, M$  represents the  $j$ th range sampling).

$a'(i,j)$  can be used to determine the mode phase  $\psi'(i,j)$  of the target return phase  $\psi(i,j)$ , where  $(-2\pi < \psi' \leq 0)$ .

When there is a relatively isolated scatterer in the target (i.e., an isolated point), it is assumed that the target range measured corresponds to the range of the isolated point. Assuming that random error in range measurement is totally due to thermal noise, then the error  $\epsilon_R(i)$  obeys a normal distribution  $N(0, \sigma_R)$ , where  $\sigma_R$  is the rms (root mean square) value of the normal distribution. When  $2\sigma_R = \delta_R/2$ , i.e.,  $\sigma_R = \delta_R/4$ , the probability of aligning the return to the same range unit  $\delta_R$  is 95.45 percent.<sup>5</sup> Because the accuracy of ranging cannot meet the above requirement, it is necessary to perform range alignment for each return. [passage omitted]

### III. Computer Simulation and Analysis of Results

With reference to a six-point model, as shown in Figure 1, computer simulation was done using the method described above. The ratio of points (1) through (6) is 1:1:1:0.5:0.6:0.8. Each point is rigidly connected and the points are equally spaced. Let us assume that the target height is  $Y_0 = 8,000$  m and the vertical distance is  $Z_0 = -39.192$  km, then, the nearest range is  $R_0 = 40$  km, as shown in Figure 2. Assuming that the target is moving linearly from point A to B at a constant speed of  $V_1 = 250$  m/s, as shown in Figure 3, then  $AB = V_1 T = 250$  m/s  $\times$  4 s = 1,000 m. The transverse resolution is

$$\delta_a \approx \frac{\lambda}{2\Delta\theta} \approx \frac{\lambda}{2AB/R_0} \approx 1\text{m} \quad (22)$$

Here, the signal-to-noise ratio (SNR) is defined as the average SNR of the element of return with the strongest average power:

$$\text{SNR} \triangleq \max \left\{ \frac{1}{N} \sum_{i=1}^N |a(i,j)|^2 / \sigma_n^2 \right\} \quad (23)$$

where  $1 \leq j \leq M = 64$ ,  $N = 400$  and  $\sigma_n^2$  is the standard deviation of noise.

Figures 4-6 show the results obtained at different SNRs. The result shown in Figure 6 is considerably worse than those shown in Figures 4 and 5. Furthermore, there is target movement in the longitudinal direction. This is because of an error in the expansion of the ambiguous Doppler frequency at lower SNRs which causes the linearly varying Doppler frequency to have an abrupt discontinuity (up or down), as shown in Figure 7. The dotted line in the figure represents the original linear Doppler frequency and the solid line indicates the discontinuity. This causes a relatively large error when we reconstruct the range and consequently produces more

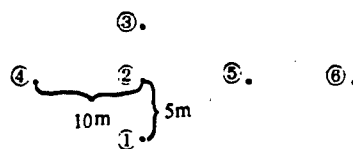


Figure 1. Target Model

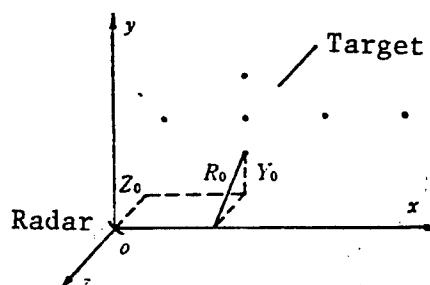


Figure 2. Relative Position Between Radar and Target

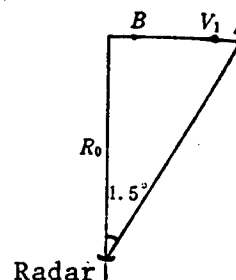


Figure 3. Target Trajectory

error in range alignment. Of course, this makes it impossible to produce an accurate image of the moving target. As for the cause of the error in Doppler frequency expansion, it is due to the fact that the noise-to-signal ratio is too high in some instances. There is a large error in the ambiguous Doppler frequency derived from the phase of the return which leads to an erroneous Doppler frequency expansion. Further study on this issue and more effective expansion of Doppler frequency will be discussed in a later article.

On the basis of the above discussion, in order to reconstruct the trajectory of a moving target, the unambiguous Doppler frequency should be accurately estimated first. When the target contains a relatively isolated and strong scatterer, the key issues in ISAR imaging are how to perform range alignment for every return wave and how to find the range element for the isolated scatterer.

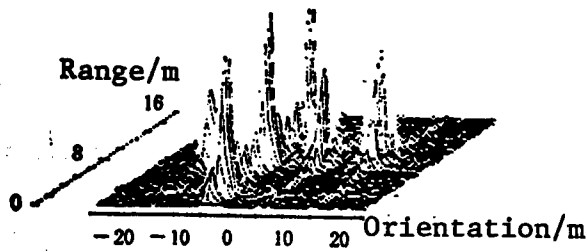


Figure 4. SNR = 30 dB

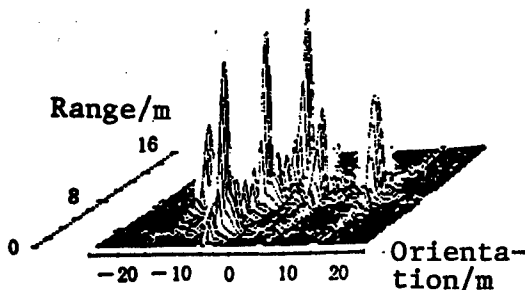


Figure 5. SNR = 20 dB

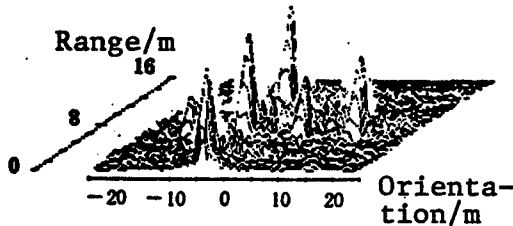


Figure 6. SNR = 15 dB

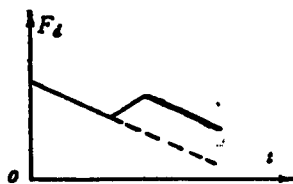


Figure 7.

#### IV. Conclusions

Under the premise that the target has a relatively isolated and intense scatterer, this paper presents a way to estimate the Doppler frequency of the return by its phase and introduces a novel method to resolve any Doppler ambiguities. Unambiguous Doppler frequency is then used to reconstruct the trajectory of the moving target to perform range alignment for every return. Furthermore, the isolated scatterer is located based on the least square

of normalized return amplitudes. The phase of the isolated scatterer is then used as the standard to compensate for the phase of the return from each range element. This method has been found to be effective through theoretical analysis and computer simulation. However, when such an isolated scatterer does not exist, or even when such an isolated point exists but the required transverse resolution is high, this phase compensation method is no longer effective. This problem will be discussed in future articles.

#### References

1. B. D. Steinberg, "Microwave Imaging of Aircraft," *PIEEE*, Vol 76, No 12, 1988.
2. C. C. Chen and H. C. Andrews, "Target-Motion-Induced Radar Imaging," *TIEEE*, Vol AES-16, No 1, 1980.
3. B. D. Steinberg, "Microwave Imaging With Large Antenna Arrays," John Wiley & Sons Inc., 1983.
4. B. D. Steinberg, D. L. Carlson and W. Lee, "Experimental Localized Radar Cross Section of Aircraft," *PIEEE*, Vol 77, No 5, 1989.
5. Edited by Fudan University, "Probability (Vol 1)," People's Education Publishing House, Beijing, 1979.

#### Meng Jing

Born in 1964 in Chengdu, he received his Bachelor of Science degree from the Department of Radio at Sichuan University. In 1987, he earned his Master's degree in communications and electronic systems from the Department of Electronic Technology at the National Defense University of Science and Technology. He is working on his Ph.D. degree in information and information processing at the Department of Electronic Technology of Xidian University. He has been involved in the study of ship target identification, and is now engaged in ISAR imaging and motion compensation studies.

#### Zhang Zhizhong

A graduate of the Department of Electrical Engineering of Zhejiang University in 1940, he was an engineer at Chongqing Telecommunications Plant and an Associate Professor in the Department of Electrical Engineering at Chongqing University until 1950. Since 1951, he has been working in the Fourteenth Research Institute at Nanjing. He worked in the capacity of Senior Engineer and is now a technical consultant. Since 1983, he has taught part time at Beijing Institute of Technology, Xidian University, and UEST as Professor and Doctoral Advisor. He has been a board member of the Chinese Society of Electronics, Chairman of the Radar Society and Chairman of Jiangsu Society of Electronics. Presently, he is a Councilman and an Honorable Member of the Chinese Society of Electronics.

## Approach to Superresolution Range-Doppler Imaging

92FE0854A Beijing DIANZI XUEBAO  
[ACTA ELECTRONICA SINICA] in Chinese  
Vol 20 No 7, Jul 92 pp 1-6

[Article by Zhu Zhaoda [2612 0340 6671], Ye Zhenru [0673 5550 1172], and Wu Xiaoqing [6762 1420 7230] of Nanjing Aeronautical Institute: "An Approach to Superresolution Range-Doppler Imaging"; supported by the National Aeronautics Foundation; MS received 5 Jan 91, revised Nov 91]

### [Text] Abstract

It is well known that the range resolution and cross-range resolution of a range-Doppler imaging radar are determined by the effective bandwidth of the transmitted signal and the angle of rotation of the object relative to the line-of-sight of the radar during the coherent processing period. The purpose of this work is to lift the limitation of conventional FFT [fast Fourier transform] range-Doppler processing to significantly improve the resolution of a range-Doppler imaging radar. The approach adopted is to use linear prediction for data extrapolation before performing Fourier reconstruction. Preliminary results of rotating platform imaging obtained in a microwave anechoic chamber indicate that this is a promising technique to enhance the resolution of range-Doppler imaging radar.

Key Words: radar imaging, superresolution processing, linear prediction, data extrapolation.

### I. Introduction

There are a variety of range-Doppler radars for different applications. Synthetic aperture radar (SAR) mounted on a moving platform is used in air-to-ground imaging. Inverse synthetic aperture radar (ISAR) fixed on the ground is used in the imaging of airplanes, space objects and heavenly bodies. A rotating platform radar is also fixed on the ground. It can also be used in imaging targets on the rotating platform. These range-Doppler radars have a common critical parameter, i.e., resolution of image reconstruction.

A range-Doppler radar gets the required resolution from the range-Doppler principle.<sup>1</sup> The range resolution of the image,  $\rho_r$ , is dependent upon the effective bandwidth of the transmitted signal B:

$$\rho_r = C/2B \quad (1)$$

where C is the speed of light. On the other hand, the cross-range resolution,  $\rho_c$ , is dependent upon the angle  $\Delta\theta$  through which the object rotates relative to the radar line-of-sight (RLOS) in the coherent processing period. The relation between  $\rho_c$  and  $\Delta\theta$  is as follows:

$$\rho_c = \lambda/2\Delta\theta \quad (2)$$

where  $\lambda$  is the radar wavelength. It should be pointed out that equations (1) and (2) are rigorously valid only when the  $\Delta\theta$  is so small that the scattering point of the target does not go over a range resolution unit and a Doppler resolution unit. With classic signal processing techniques, it is impossible to overcome this limitation imposed by equations (1) and (2). In this case, the effective bandwidth of the transmitted signal and the total angle of rotation of the target with respect to the RLOS must be increased to enhance the range resolution and cross-range resolution of the image, respectively. It is often not desirable to do so in many applications. Another approach to improving the resolution capability is to use advanced, rather than conventional, signal processing methods because these methods may be able to enhance the range resolution to a level that far exceeds the limitation discussed earlier.

Signal processing in range-Doppler imaging can be considered as a two-dimensional spectral analysis problem. Many high-resolution spectral estimation and frequency estimation methods, i.e., modern spectral estimation methods, have been studied.<sup>2</sup> In order to take advantage of the superiority of these methods, an accurate signal model and a sufficient signal-to-noise ratio (SNR) are required. Furthermore, modern spectral estimation methods are far more complex compared to the classical Fourier method. For this reason, people continue to investigate methods that combine modern high-resolution techniques with the classical approach. One of the hybrid approaches<sup>3</sup> is relatively simple in concept and in computation. In this approach, a linear prediction filtering method is employed to extrapolate the data beyond the observation window. Then, the extrapolated data undergoes discrete Fourier transform (DFT) to attain a higher frequency resolution. This method is used to improve the resolution of rotating platform imaging to construct a two-dimensional image of a B-52 model by processing data obtained in a microwave anechoic chamber. Preliminary results indicate that this superresolution range-Doppler radar imaging method is less complex in computation and more general in applicability. In the area of modern spectral estimation methods to improve radar imaging resolution capability, Gabriel<sup>4,5</sup> introduced a maximum likelihood filter method and a linear prediction filter method to achieve superresolution range-Doppler imaging. These methods involve the determination of the inverse of matrices, which requires a great deal of computation. Furthermore, references 4 and 5 only provided imaging results of simulated data and did not verify the methods with measured data.

In this paper, the use of linear prediction for data extrapolation to achieve superresolution imaging is described first. A similar method is then used to obtain superresolution of cross-range imaging. Finally, a superresolution two-dimensional image of a B-52 model is presented.

## II. Superresolution Range Imaging

The high range-resolution capability needed in range-Doppler radar imaging can be realized by using techniques such as bandwidth pulse compression, time-bandwidth interchange, or frequency-stepping waveform. The method described here is also applicable to pulse compression and time-bandwidth interchange. The difference is that the pre-treatment is slightly different.<sup>1,6</sup>

When frequency-stepping waveform is employed, the radar transmission frequency and the receiver local-oscillation frequency vary in a stepwise manner. Figure 1 shows a target at a distance R away from the radar;  $f(r)$  is the range function of the reflectivity of the target. It is also known as the range image of the target. The variable  $r$  represents the distance of the target with respect to the reference point  $o$ . With a specific viewing angle, the radar transmits a series of K pulses at a frequency

$$f_k = f_0 + k\delta f, k = 0, 1, \dots, K - 1. \quad (3)$$

The return from the target after compensating for the

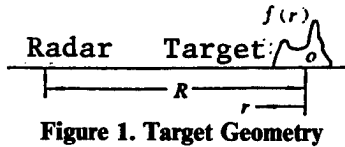


Figure 1. Target Geometry

phase term due to range R can be expressed as follows:

$$S_k = A \int f(r) \exp \left\{ +j \frac{4\pi}{C} f_k r \right\} dr, \quad k = 0, 1, \dots, K - 1. \quad (4)$$

where A is a proportionality factor which is dependent upon factors such as power and signal transmission. It is also assumed the pulse width covers the entire target range. Integration is carried out along  $r$  over the entire target range. Equation (4) implies that  $S_k$  is the inverse Fourier transform of  $f(r)$ . Hence, after knowing the K vector of  $S_k$ , it is possible to estimate  $f(r)$  by computing the DFT of  $S_k$  where  $k = 0, 1, \dots, K - 1$ . Obviously, the range resolution of such a target image is

$$\rho_r = C/2K\delta f \quad (5)$$

This is consistent with equation (1) because here the effective bandwidth of the transmitted signal is  $B = K\delta f$ .

Let us assume that the scattering from an extended target comes from a finite number of scattering centers.<sup>7</sup> For an individual scattering center, if its range is  $r_0$ , the observed signal in the frequency domain is a complex sine function of

$$Af(r_0) \exp \left\{ +j \frac{4\pi}{C} r_0 f \right\}$$

Therefore, the observed signal of the target is comprised of a series of complex sine functions in the frequency domain. It can be accurately predicted by a linear prediction filter of an order equal to or greater than the number of complex sine functions.<sup>2</sup> Although this statement is valid only when there is no noise in the observed signal, in reality it is still possible to employ linear prediction to reliably extrapolate the data outside the observation window when the SNR is relatively low.

Assuming that actual data  $S_k, k = 0, 1, \dots, K - 1$ , has been obtained at a given viewing angle, a single-step linear prediction filter of order P is used to extrapolate the data. The filter coefficient is  $a_p, p = 1, \dots, P$ . This filter produces a forward extrapolation sample  $S_k$  as follows:

$$S_k = \sum_{p=1}^P S_{k-p} a_p, \quad k > K \quad (6)$$

The backward extrapolation process is similar. The difference is that the filtering direction is reversed. Moreover, the filter coefficients are complex conjugates of those of the forward filter. In other words, the extrapolation takes place according to the following:

$$S_k = \sum_{p=1}^P S_{k+p} a_p^*, \quad k < 1 \quad (7)$$

Thus, the data is actually measured if  $1 \leq k \leq K$  and the data is extrapolated when  $k > K$  and  $k < 1$ . The forward extrapolation length is equal to that of backward extrapolation. The Burg maximum entropy (ME) technique is used to calculate coefficients  $a_p, p = 1, \dots, P$ . A vector with N data points ( $N > K$ ) can be obtained with the method described above. This N-point extrapolated vector replaces the original K-point vector in the DFT computation. The range image thus derived can be expected to have a much better range resolution.

Figure 2 shows the overall range image of a B-52 model. This is the result of computer processing based on microwave anechoic chamber data. A frequency stepping technique was used in the experiment. The number of frequency steps is  $K = 32$ . The transmitted signal has an effective bandwidth of  $B = 2.15$  GHz. Table 1 shows the raw data obtained in the microwave anechoic chamber at a specific viewing angle. Figures 2(a) and (b) are the range images obtained with the original 32 data points and with 128 extrapolated points with a Hamming window, respectively. It is apparent that data extrapolation by linear prediction, in conjunction with conventional Fourier transformation, can provide super-resolution range images.

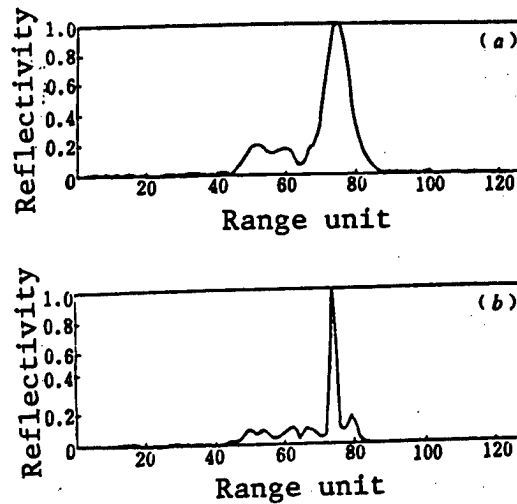


Figure 2. Range Image of B-52 Model at a Specific Viewing Angle. (a) with 32 original points, (b) with 128 extrapolated points

Table 1. Raw Data at a Specific Viewing Angle

|          |         |         |         |         |         |         |         |
|----------|---------|---------|---------|---------|---------|---------|---------|
| -.080 99 | .11520  | -.12826 | .10653  | -.17118 | .07572  | -.19275 | .00786  |
| -.169 40 | -.08068 | -.13269 | -.18262 | -.06945 | -.26023 | -.01409 | -.27528 |
| .048 96  | -.21143 | .08769  | -.08913 | .09758  | .06676  | .08207  | .19537  |
| .026 67  | .26618  | -.04690 | .25384  | -.11979 | .18449  | -.17199 | .06819  |
| -.184 57 | -.05550 | -.16452 | -.14741 | -.10523 | -.19206 | -.02174 | -.19634 |
| .064 16  | -.17319 | .13968  | -.12860 | .19338  | -.08315 | .21725  | -.03815 |
| .214 41  | .01149  | .16985  | .06559  | .11442  | .13303  | .05429  | .17366  |
| -.015 34 | .17477  | -.07138 | .13274  | -.11886 | .03660  | -.14958 | -.06196 |

### III. Superresolution Cross-Range Imaging

In small-rotation-angle imaging with the FFT range-Doppler process, range and cross range are processed separately. As described in Section II, we can obtain a range image at every viewing angle. At  $M$  equally spaced viewing angles,  $M$  range images of the target can be obtained. Thus, a data vector of  $M$  points can be obtained with respect to each range unit. The cross-range image of a given range unit, i.e., the reflectivity of the target in that range unit as a function of the cross range, can be derived from the DFT of this  $M$ -point vector. When it is applied to a sample of  $M$  actually measured data points, the cross-range resolution is

$$\rho_c = \lambda/2M\delta\theta \quad (8)$$

where  $\delta\theta$  is the spacing of two neighboring viewing angles. Since  $\Delta\theta = M\delta\theta$ , equation (8) is consistent with equation (2).

On the basis of the same argument to attain super range resolution discussed in Section II, superresolution cross-range images can be obtained by using linear prediction for data extrapolation in conjunction with conventional Fourier transformation. Figure 3 shows the overall cross-range image of the B-52 model at a range unit derived from measured data. The total angle of rotation of the airplane model in the imaging process is  $\Delta\theta = 15^\circ$  and the radar wavelength is  $\lambda = 2$  cm. Table 2 lists the 32 original data points corresponding to the range unit. Figures 3(a) and (b) show the result obtained from the original 32 data points and that derived from the 128 extrapolated points with a Hamming window, respectively. It is apparent that using linear prediction for data extrapolation can also significantly improve the cross-range resolution of range-Doppler radar imaging.

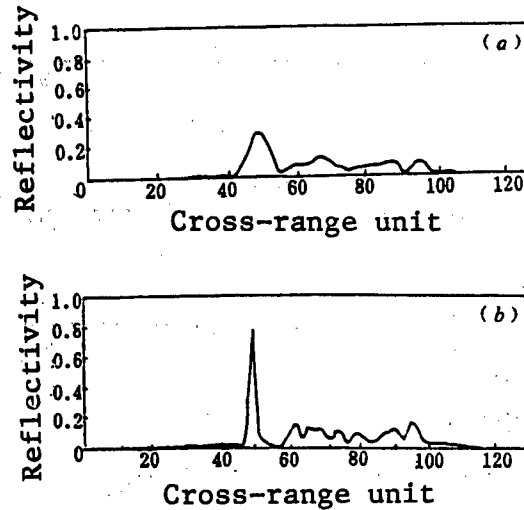


Figure 3. Cross-Range Image of B-52 Model. (a) with 32 original points, (b) with 128 extrapolated points

Table 2. Raw Data at a Given Range Unit

|          |         |          |         |         |         |         |         |
|----------|---------|----------|---------|---------|---------|---------|---------|
| .391 29  | .43871  | -.07534  | -.23074 | .50295  | -.80743 | .53297  | -.65919 |
| -.569 85 | -.42205 | -1.20443 | -.69226 | -.40890 | -.36944 | .21238  | .43367  |
| .303 96  | .82409  | .19226   | .46031  | .17158  | -.13421 | .11666  | -.61985 |
| -.097 28 | -.70557 | -.27174  | -.52000 | -.16635 | -.05365 | .10964  | .39470  |
| .395 75  | .54619  | .62743   | .19806  | .82085  | -.28259 | .75538  | -.51553 |
| .319 49  | -.41673 | -.17068  | -.27398 | -.13106 | -.10458 | .21626  | .16420  |
| .479 72  | .42178  | .43015   | .29670  | .23022  | -.15925 | .01776  | -.47091 |
| -.237 82 | -.43817 | -.51430  | -.18886 | -.53399 | -.04538 | -.26843 | -.02514 |

#### IV. Superresolution Two-Dimensional Imaging

The range resolution and cross-range resolution in two-dimensional range-Doppler imaging can both be improved with the method described above. The results are shown in Figure 4. Using the data shown in two previous sections, a two-dimensional radar image of the airplane model was obtained by processing the range dimension first for every viewing angle and then processing the cross range for every range unit. Figures 4(a) and (b) show the images of the B-52 model processed based on the original 32 x 32 data matrix and the extrapolated 128 x 128 matrix, respectively. A comparison shows that our approach significantly improved range resolution and cross-range resolution of the image. Compared to the photograph of the B-52 model shown in Figure 5, the two engines under the wing were clearly visible in the superresolution two-dimensional image shown in

Figure 4(b).

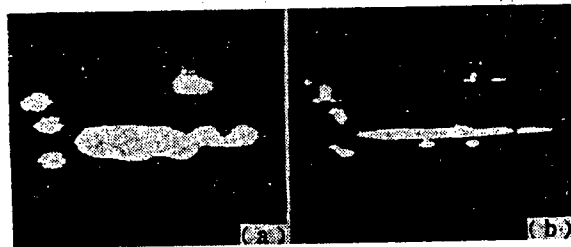


Figure 4. Two-Dimensional Image of B-52 Model. (a) 32 x 32 true data matrix, (b) 128 x 128 extrapolated data matrix



Figure 5. Photograph of B-52 Model

The microwave anechoic chamber data used has a very high SNR. It almost can be treated as a noise-free case. In order to investigate the effect of SNR on the superresolution imaging technique described, white Gaussian noise was added to the microwave anechoic chamber data. A great deal of results indicate that this method can still produce better superresolution two-dimensional images even with a low SNR. Figure 6 shows the results with an SNR of 0 dB.



Figure 6. Two-Dimensional Images of B-52 Model With SNR = 0 dB. (a) 32 x 32 true data matrix, (b) 128 x 128 extrapolated data matrix

## V. Conclusions

Our preliminary results indicate that superresolution range-Doppler radar imaging using data extrapolation via linear prediction is a relatively simple and practical superresolution imaging method. It is capable of lifting the resolution limitation of conventional Fourier image processing. This method can produce higher resolution images with identical effective transmission bandwidth and total angle of rotation during imaging. Or, it can produce an image of similar resolution with a smaller bandwidth and total rotation angle.

During the process of revising this paper, the authors found that Li<sup>8</sup> et al. used a similar method to improve the resolution in one-dimensional range imaging by extrapolating data in different isolated segments. This work has presented a method for two-dimensional superresolution range-Doppler imaging. In addition, the effect of SNR on this method has also been studied. Even with a low SNR, this method was still found to be capable of producing better superresolution two-dimensional images.

The authors wish to express their gratitude to Professors Liu Yongtan [0491 3057 0962], Cao Zhidao [2580 1807 6670], and Meng Xiande [1322 2009 1795] of Harbin Institute of Technology and to colleagues at the 207th Institute of the Ministry of Aerospace Industry for providing the microwave anechoic chamber data.

## References

1. D. A. Ausherman, et al., "Developments in Radar Imaging," IEEE TRANS. ON AEROSPACE AND ELECTRONIC SYSTEMS, July 1984, AES-20 (4): 363-398.
2. S. M. Kay, "Modern Spectral Estimation: Theory and Application," University of Rhode Island, Kingston, Rhode Island, 1988.
3. T. J. Ulrych, et al., "Predictive Filtering and Smoothing of Short Records by Using Maximum Entropy," JOURNAL OF GEOPHYSICAL RESEARCH, August 1973, 78 (23): 4959-4964.
4. W. F. Gabriel, "Superresolution Techniques and ISAR Imaging," IEEE NATIONAL RADAR CONFERENCE DIGEST, March 1989: 48-55.
5. W. F. Gabriel, "Superresolution Techniques in the Range Domain," Proc. of Intl. Radar Conference, May 1990: 263-267.
6. M. J. Prickett and C. C. Chen, "Principle of Inverse Synthetic Aperture Radar (ISAR) Imaging," IEEE 1980 EASCON Record, 1980: 340-345.
7. R. L. Mitchell, "Models of Extended Targets and Their Coherent Radar Images," PROC. OF IEEE, June 1974, 62 (6): 754-758.
8. H. J. Li, N. H. Farhat, Y. Shen, "A New Iterative Algorithm for Extrapolation of Data Available in Multiple Restricted Regions With Application to Radar Imaging," IEEE TRANS., May 1987, AP-35 (5): 581-588.

### Zhu Zhaoda

Born in 1939, he graduated from the Department of Automatic Control at Nanjing Aeronautical Institute in 1960 and remained at the institute to teach in the Department of Radio Engineering. In 1986, he was promoted to Professor of Electronic Engineering. He went to McMaster University in Canada as a visiting scholar in 1987-1988. In 1990, he was qualified as a Ph.D. adviser in communications and electronics. He is an editor of HANGKONG XUEBAO [JOURNAL OF AERONAUTICS] and XINHAO CHULI [SIGNAL PROCESSING] and is a member of IEEE. His major research areas include detection and estimation, radar signal processing and array signal processing.

### Ye Zhenru

Born in September 1936, he graduated from the Department of Aeronautical Engineering at Nanjing Aeronautical Institute in 1960. He stayed at the institute to teach in the Department of Radio Engineering. In 1987, he was promoted to Associate Professor of Electronic Engineering. His major areas of interest include detection and estimation, radar signal processing, and adaptive signal processing.

### Wu Xiaoqing

Born in August 1963, he received his Bachelor's and Master's degrees in electronic engineering from Nanjing Aeronautical Institute in 1982 and 1985, respectively.

Since 1985, he has taught at the institute in the Department of Electronic Engineering. In 1990, he was promoted to Associate Professor. His major areas of interest include radar signal processing, pattern recognition and adaptive filtering.

**Microwave Imaging of Targets Rotating in Small Azimuth Angle Range**

92FE0801E Beijing DIANZI XUEBAO  
[ACTA ELECTRONICA SINICA] in Chinese  
Vol 20 No 6, Jun 92 pp 54-60

[Article by Huang Peikang [7806 1014 1660], Xu Xiaojian [6079 1420 0494], Chao Zengming [1560 1073 2494], and Xiao Zhihe [5135 1807 3109] of Beijing Institute of Environmental Features, Ministry of Aerospace Industry, Beijing 100854: "Microwave Imaging of Targets Rotating in Small Azimuth Angle Range"; MS received Oct 90, revised Mar 91]

[Text] Abstract

The imaging of targets rotating in a small azimuth angle range is discussed. A unified image reconstruction scheme suitable for bistatic, monostatic, near-field and far-field imaging geometries is derived. Super-resolution imaging techniques are investigated. A new imaging reconstruction algorithm, combining spectral extrapolation and coarse "shape" information, is presented. Finally, experimental results in microwave anechoic chambers are described.

Key Words: microwave imaging, radar targets, imaging processing.

**I. Introduction**

Microwave imaging of rotating targets has been widely used in many areas, such as: (1) Target diagnosis and identification. Rotating target imaging is a basic tool for studying the electromagnetic scattering of targets. It plays an important role in the study of electromagnetic scattering mechanism and RCS reduction for stealth research and target identification. (2) SAR and ISAR signal processing. SAR or ISAR imaging with motion compensation is equivalent to rotating target imaging. (3) Non-destructive testing. The principle of rotating target imaging is also widely used in non-invasive and non-destructive testing. Therefore, in-depth study of rotating target imaging and related processing techniques is a basic research project with a wide range of applications.

D. L. Mensa<sup>1</sup> once pointed out that imaging of targets rotating over 360° could achieve extremely high nominal two-dimensional resolution (a fraction of a wavelength of the radar). The condition to attain such a high

resolution is that all the scatterers on the target must be isotropic. Furthermore, the scatterers must not move in order to obtain a uniform synthetic radar aperture over 360°. However, the following two reasons make rotation imaging in small azimuth angle range more practical. (1) Real radar targets often cannot satisfy the requirement that the scatterers be isotropic and stationary. Hence, it is not possible to attain the high theoretical nominal resolution. Furthermore, the amount of work involved in data acquisition and processing for 360° rotating target imaging is tremendous. (2) As radar signal technology advances, high radial resolution of the target can be obtained with a wideband signal alone. It usually takes a small azimuth angle to achieve high transverse resolution. Therefore, imaging of targets in a small azimuth angle range has been developed for a variety of applications in the past two decades.

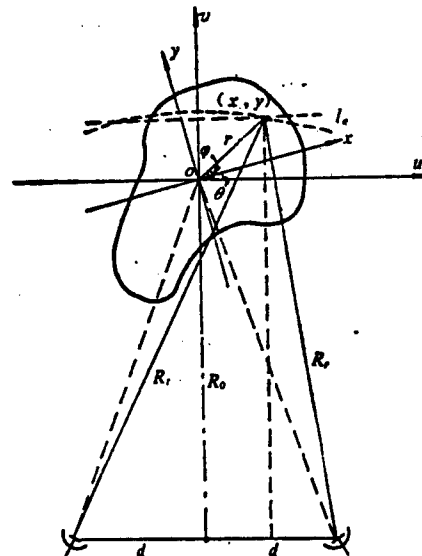
**II. Image Reconstruction Algorithm**

The bistatic geometry for rigid target imaging is shown in Figure 1. The target coordinate is (x-y) and the radar coordinate is (u-v).

$$x = u \cos \theta - v \sin \theta, \quad y = u \sin \theta + v \cos \theta \quad (1)$$

or

$$u = x \cos \theta + y \sin \theta, \quad v = -x \sin \theta + y \cos \theta \quad (2)$$



Transmission antenna      Receiving antenna  
Figure 1. Geometry for Microwave Imaging

The two-way range between a point on the target (x,y) and the transmitter and receiver is

$$\begin{aligned} R_s &= [(R_0 + v)^2 + (d + u)^2]^{1/2} \\ &= \{R_0^2 + v^2 + d^2 + 2r[R_0 \sin(\varphi - \theta) \\ &\quad + d \cos(\varphi - \theta)]\}^{1/2} \end{aligned} \quad (3)$$

$$\begin{aligned} R_r &= [(R_0 + v)^2 + (d - u)^2]^{1/2} \\ &= \{R_0^2 + r^2 + d^2 + 2r[R_0 \sin(\varphi - \theta) \\ &\quad - d \cos(\varphi - \theta)]\}^{1/2} \end{aligned} \quad (4)$$

and

$$\begin{aligned} R &= R_s + R_r \\ &= \{R_0^2 + r^2 + d^2 + 2r[R_0 \sin(\varphi - \theta) \\ &\quad + d \cos(\varphi - \theta)]\}^{1/2} \\ &\quad + \{R_0^2 + r^2 + d^2 + 2r[R_0 \sin(\varphi - \theta) \\ &\quad - d \cos(\varphi - \theta)]\}^{1/2} \end{aligned} \quad (5)$$

From the above formulas, after frequency mixing, calibration and filtering, the return can be derived as follows:

$$F(K, \theta) = \iint_{-\infty}^{\infty} f(r, \varphi) \exp\{-j\pi K(R_s + R_r - 2R_0)\} r dr d\varphi \quad (6)$$

From equation (6), the return is the correlation integral of the scattering signals along various equidistance lines;  $f(r, \varphi)$  is the scattering function of the target. In two-dimensional imaging of rotating targets, the spectral domain signal of  $f(r, \varphi)$  is measured in the ring-shaped spectral domain shown in Figure 2. The integration for image reconstruction is also performed in this domain. The image reconstruction equation expressed in polar coordinate is as follows:

$$\hat{f}(r, \varphi) = \int_{-\infty}^{\infty} \int_{\kappa_1}^{\kappa_2} F(K, \theta) K \exp\{j\pi K(R_s + R_r - 2R_0)\} dK d\theta \quad (7)$$

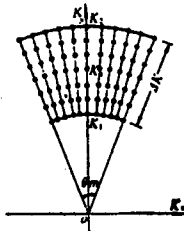


Figure 2. Polar Coordinate Data Format in Imaging of Rotating Target

Various reconstruction methods can be designed based on equation (7), including the two-dimensional Fast Fourier Transform (2-D FFT), filtered back-projection (FBP) and Fourier domain extrapolation.

Experimental and theoretical studies indicate that the FBP method not only is more flexible but also produces higher quality reconstructed images in two-dimensional imaging of rotating targets. It is suitable for anechoic chamber imaging. This method is described as follows:

In equation (7), if the integration of  $K$  is treated as the inverse Fourier transform of variable  $l_e = (R_s + R_r - R_0)/2$ , then the reconstructed  $f[\text{cart}](r, \varphi)$  becomes

$$\begin{aligned} P_s(l_e) &= \int_0^{\kappa_2 - \kappa_1} |K + K_1| F(K + K_1, \theta) \\ &\quad \exp\{j2\pi K l_e\} dK \\ \hat{f}(r, \varphi) &= \int_{-\infty}^{\infty} P_s(l_e) \exp\{j2\pi K_1 l_e\} dl_e \\ l_e &= (R_s + R_r - R_0)/2 \end{aligned} \quad (8)$$

In actual computation, the first formula (radial focusing) is computed by FFT and then the second formula is used to compute back-projection (transverse focusing). It is very similar to the FBP technique in tomographic imaging. Hence, it is also called filtered back-projection.<sup>2-4</sup>

The third formula in equation (8) describes the path of back-projection. From analytical geometry, the path of back-projection described by that formula follows an elliptical trajectory. It is identical to the integration path of radar projection measurement, i.e.,

$$\begin{aligned} l_e &= \{[R_0^2 + r^2 + d^2 + 2r(R_0 \sin(\varphi - \theta) \\ &\quad + d \cos(\varphi - \theta))]\}^{1/2} \\ &\quad + [R_0^2 + r^2 + d^2 + 2r(R_0 \sin(\varphi - \theta) \\ &\quad - d \cos(\varphi - \theta))]\}^{1/2} - 2R_0\} / 2 \end{aligned} \quad (9)$$

If it is a monostatic measurement, then in Figure 1  $d = 0$  and equation (9) becomes

$$l_e = [R^2 + r^2 + 2r R_0 \sin(\varphi - \theta)]^{1/2} - R_0 \quad (10)$$

This describes a family of circles. In other words, in monostatic measurements, the projection integration path is a circular arc and the back-projection path in image reconstruction is also circular.

Furthermore, when  $R_0 \gg r$ , i.e., the far-field condition is met, then

$$l_e \approx r \sin(\varphi - \theta) \quad (11)$$

Equation (11) describes a straight line. It is suitable in far-field imaging (plane wave front).

The derivation of equation (8) does not require the radar to emit plane electromagnetic wave fronts. Therefore, the resultant reconstruction method is applicable to a variety of imaging conditions such as monostatic, bistatic, far-field and near-field. Incidentally, because the target spectrum obtained in microwave imaging of a rotating target is located in a ring-shaped domain, the expansion function of the imaging system has very high side lobes. Therefore, usually a smoothing window (at small azimuth angle) or variable trajectory filter (360° imaging)<sup>5</sup> is required in the actual reconstruction computation to suppress the side-lobe voltage in the reconstructed image to improve image quality.

### III. Super-Resolution Imaging Technique

It is well known that linear prediction is widely used in the estimation of high-resolution power spectrum of a discrete time sequence, especially when the sequence is very short. By means of extrapolating the sequence, it is possible to achieve higher resolution than that of a conventional Fourier spectrum. Since in microwave imaging the two-dimensional resolution is determined by the frequency spectrum window and azimuth window, when the radar bandwidth is narrow or the azimuth angle is small, the resolution deteriorates rapidly. In order to obtain a high-resolution microwave image with a small amount of data, linear prediction is used to investigate the super-resolution imaging of microwave data.

Based on the Burg algorithm,<sup>6,7</sup> a sequence with  $M$  specimens  $[x_1, x_2, x_3, \dots, x_m]$  is extrapolated by linear prediction to have  $N$  ( $N > M$ ) specimens. The prediction parameters can be obtained by minimizing the sum of errors in energy,  $E_p$ , of forward and backward prediction, i.e.,

$$E_p = \sum_{j=p}^{N-1} |E_{pf}|^2 + \sum_{k=p}^{N-1} |E_{pb}|^2 \quad (12)$$

where  $E_{pf}$  is the forward prediction error of the  $p$ th order model:

$$E_{pf} = \sum_{k=0}^p a_{pk} x_{n-k} \quad (13)$$

and  $E_{pb}$  is the backward prediction error of the  $p$ th order model:

$$E_{pb} = \sum_{k=0}^p a_{pk}^* x_{n-p-k} \quad (14)$$

Here,  $a_{pk}$  is the linear prediction parameter and \* represents a complex conjugate operation.

The linear prediction equation for extrapolation with  $M$  specimens is as follows:

$$\hat{x}_{M+j} = \sum_{k=1}^p a_{pk} x_{M+j-k} \quad j > 0 \quad (15)$$

$$\hat{x}_{-j} = \sum_{k=1}^p a_{pk}^* x_{-j+k} \quad j > 0, \quad (16)$$

where [caret] represents the estimated value.

Figure 3 shows schematic diagrams of one- and two-dimensional extrapolation by linear prediction with partial data in the target spectrum. After spectral expansion, the image can be reconstructed with the resultant data using the method described in the last section to obtain a super-resolution image of the target.

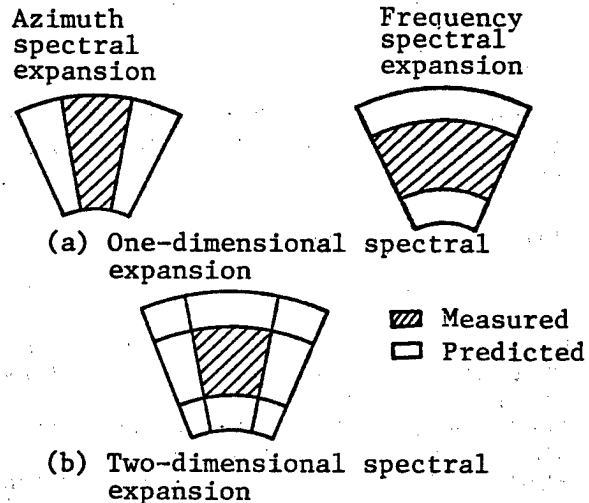


Figure 3. Image Spectrum Expansion by Linear Prediction

In image reconstruction with extrapolated data by linear prediction, it was found that although the resolution is enhanced, the side-lobe voltage of the image is also increased due to prediction errors. In order to suppress image side lobes, an algorithm is developed to combine linear prediction with the rough "shape" of the target. The "shape" is derived from the original data. Specifically, both original data and extrapolated data are processed in image reconstruction. In radial focusing with FBP, two sets of range distribution plots are obtained. The range distribution plot obtained from the extrapolated data is compared to that derived from the original data to eliminate the side lobes. After both images are reconstructed, comparison can be made again to further eliminate any side lobes other than the "shape" of the target in the original image. This new algorithm can drastically lower the side-lobe voltage of the image.

Figure 4 shows the flowchart of this method. The results will be presented in the next section.

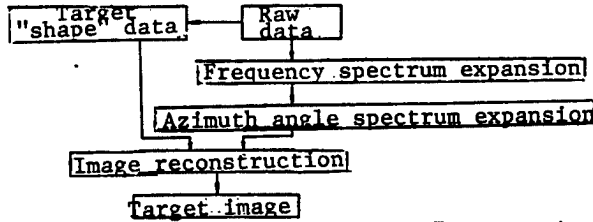


Figure 4. Flowchart of the New Image Reconstruction Algorithm

#### IV. Anechoic Chamber Experiments and Results

The entire experiment was done on the microwave measurement and imaging system of an HP8510 network analyzer. The major specifications of the system are shown in Table 1.

Table 1. Major Specifications of the Microwave Imaging System

|                                   |   |
|-----------------------------------|---|
| Sweep range                       | 2-4, 4-8, 8-18 GHz  |
| Frequency stability               | $1 \times 10^{-9}$ /day                                   |
| Output power                      | 20 dBm  |
| Antenna gain                      | 23 dB   |
| Rotating platform accuracy        | 0.05°   |
| Minimum step of rotating platform | 0.1°  |
| Amplitude measurement accuracy    | +/- 0.5 dB  |
| Sweep linearity                   | 1% in sweeping mode                                       |
| Sweep mode                        | Stepping, sweeping  |
| Receiver sensitivity              | -85 dBm (unaveraged)<br>-103 dBm (averaged over 64 times) |
| Dynamic range                     | 75 dB (unaveraged)<br>93 dB (averaged over 64 times)      |
| Phase measurement accuracy        | +/- 3°  |

During the imaging process, a microcomputer controls the transmitter, receiver and azimuth angle. The amplitudes and phases of the wide-band scattered returns from the target are collected at different azimuth angles. The data gathered is also pre-processed by the microcomputer.

The pre-processing, including software range gate technology for background cancellation, data scaling and clutter filtering outside the target range, can be expressed by the following equation:

$$C = E \frac{\mathcal{F}\{T - B_s\}}{\mathcal{F}\{S - B_s\}} = E \frac{T_i}{S_i} \quad (17)$$

where  $E$  is the accurate amplitude phase of the calibrator,  $T$  is the frequency-domain measurement of the target,  $T_i$  is the intrinsic scattering of the target,  $S$  is the frequency-domain measurement of the calibrator,  $S_i$  is the inherent scattering of the calibrator,  $B_s$  is the background during target measurement,  $B_c$  is the background during scalar measurement, and script  $\mathcal{F}[\ ]$  represents the filtering process.

The RCS amplitude of the pre-processed imaging data can be expressed in dB referenced to a square meter (dBsm). The phase is centered around the rotating platform. The data is then used for image reconstruction and image output by a microcomputer.

Figure 5 shows the resultant image of a reduced B52 model in an anechoic chamber. The experimental conditions are: center frequency 11.5 GHz, radar bandwidth 7.0 GHz, frequency step 35 MHz, target rotation angle 20°, angular sampling interval 0.5°, antenna polarization state H-H, test range 12.5 m. A Hamming window was added in image reconstruction. The specifications attained are: radial resolution approximately 4 cm, transverse resolution 7 cm, and image side-lobe voltage less than -40 dB. The dynamic range of the imaging system is actually limited by the side-lobe voltage. The dotted line in the figure represents the actual silhouette of the reduced model. Its scattering center and the contour lines obtained from imaging are in excellent agreement.

Figures 6 and 7 show the reconstructed images derived from the raw data and the two-dimensional extrapolated data, respectively. Some data were acquired with a reduced bandwidth of 3.5 GHz and smaller azimuth angle of 15°. Comparing Figure 7 to Figure 5, we find that the resolution of the reconstructed image from the raw data and that of the reconstructed image based on extrapolated data are essentially the same. However, there is some error in the amplitude of the scattering center (approximately 1-2 dB).

#### V. Conclusions

(1) Using a 7 GHz wide-band frequency spectrum and 20° rotation angle aperture imaging, it is possible to obtain a high-resolution microwave image of the order of a centimeter.

(2) The FBP algorithm derived is applicable to a variety of imaging geometries and conditions including bistatic, monostatic, near-field and far-field.

(3) By combining spectral expansion and target rough-shape data, super-resolution imaging can be attained. Consequently, the amount of imaging data required is drastically reduced. At 3.5 GHz and 15° azimuth window, the resolution is almost as high as at 7 GHz and 20° azimuth window, and side-lobe voltage is better than -40 dB. However, there is some error in amplitude.

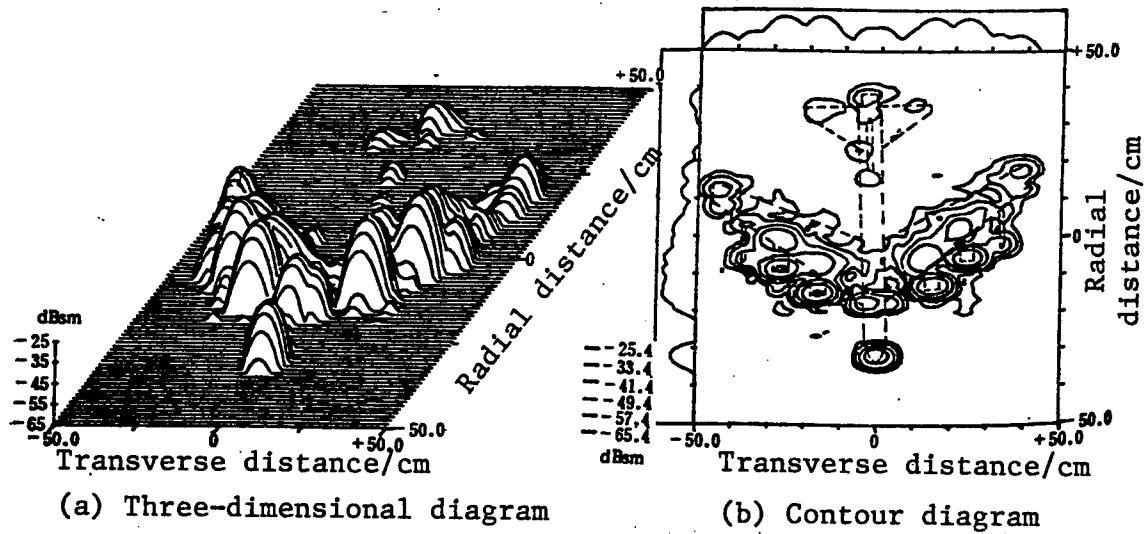


Figure 5. Imaging of a B52 Model

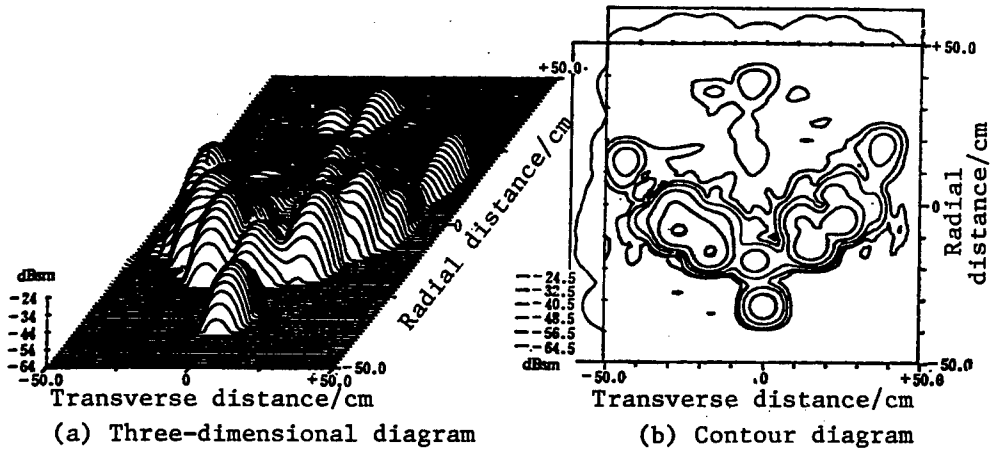


Figure 6. Image Reconstructed From Raw Data

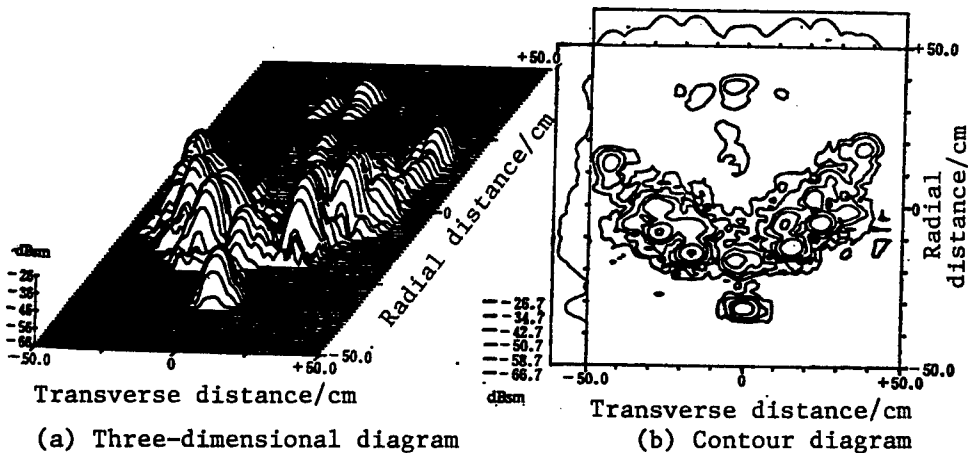


Figure 7. Image Reconstructed From Spectral Expanded Data

Finally, in addition to spectral expansion, the quality of the image may be further improved by using polarization information and target symmetry. This effort is in progress.

#### References

1. D. L. Mensa, "High-Resolution Radar Imaging," ARTECH HOUSE, Inc., 1981.
2. M. Desai, et al., "Convolution Back-Projection Imaging Reconstruction for SAR," ISCAS'84, p 261.
3. Xu Xiaojian, "Coherent Tomographic Microwave Imaging of Rotating Target," Master's Thesis, Beijing, Ministry of Astronautics Industry, February 1986.
4. Xiao Zhihe, "Microwave Imaging of Rotating Target by Filtering and Back-Projection," Master's Thesis, Beijing, Ministry of Aerospace Industry, January 1989.
5. Huang Peikang and Xu Xiaojian, "Side-Lobe Suppression in Microwave Imaging of Rotating Target," YUHANG XUEBAO [JOURNAL OF THE CHINESE SOCIETY OF ASTRONAUTICS], Vol 4, 1988.
6. J. P. Burg, "A New Analysis Technique for Time Series Data," NATO Advanced Study Institute on Signal Processing With Emphasis on Underwater Acoustics, August 1968.
7. H. J. Li, et al., "A New Iterative Algorithm for Extrapolation of Data Available in Multiple Restricted Regions With Application to Radar Imaging," IEEE TRANS., Vol AP-35, No 5, 1987, pp 581-588.

#### Huang Peikang

Born in 1936, he graduated from the Department of Radio Engineering at Nanjing Institute of Engineering in 1956. He is the Chief Engineer, Research Fellow and Professor at Beijing Institute of Environmental Features, Ministry of Aerospace Industry. Earlier in his career, he conducted research in radar system engineering and electronic warfare. He is actively involved in national high-technology projects in areas such as radar targets, microwave remote sensing, high-resolution imaging, target identification and space electronics.

#### Xu Xiaojian

Born in 1963, he graduated from the Department of Electronic Engineering at Hefei Polytechnic University in 1983. He received his Master's degree from Beijing Institute of Environmental Features in 1986 and is a Senior Engineer at that institution. His areas of specialty include extraction of target characteristics, microwave imaging, signal analysis, image processing and mode identification.

#### Chao Zengming

Born in 1963, he graduated from the Department of Physics at Jiangxi University and received a Master's degree from Beijing Institute of Environmental Features.

He is currently employed as an engineer at the target electromagnetic scattering laboratory. His areas of research are radar targets, scattering measurement and processing of target characteristics.

#### RCS Analysis of Slot-Array Antennas

92FE0801B Beijing DIANZI XUEBAO  
[ACTA ELECTRONICA SINICA] in Chinese  
Vol 20 No 6, Jun 92 pp 15-20

[Article by Deng Shuhui [6772 2579 6540] and Ruan Yingzheng [7086 4481 6927] of Chengdu University of Electronic Science and Technology (UEST): "Radar Cross Section Analysis of Slot-Array Antennas"; MS received Oct 90, revised Jul 91; project supported by the doctorate fund of the State Education Commission and the Institute of Electronic Science of the Ministry of Machine-Building and Electronics Industry]

#### [Excerpts] Abstract

In this work, the scattering of a large planar slot-array antenna is studied using the momentum method, physical optics method and singularity elimination technique. The radar cross section (RCS) of a typical array was calculated and verified experimentally. It is found that the calculated result is in good agreement with the experimental data. The computations also show that the contribution of the plane to the scattering field (structure term) is far greater than that of the slot (mode term).

Key Words: planar slot-array antenna, radar cross section, scattering.

#### I. Introduction

The large planar slot-array antenna is one of the commonly used airborne antennas. However, it produces a very strong RCS contribution in the direction of the nose of the aircraft. In order to improve the stealth characteristics of the aircraft, it is necessary to understand the scattering mechanism of this type of antenna and analyze and calculate its RCS contribution. To date, most of the studies on the coupling of incident wave and slot-array antenna, or scattering computation, involved the combination of a single slot and a cavity.<sup>1-3</sup> There is no information available on the scattering mechanism of a large planar slot-array antenna and the detailed analysis of its RCS. This work provides a theoretical analysis of this type of antenna by rigorously taking the interaction between elements into consideration using momentum method, physical optics method and singularity elimination technique. Moreover, the computing time is drastically reduced through the use of symmetry technique, Toeplitz property and an excellent inverse technique.

#### II. Antenna Array Analysis

Figures 1 and 2 show the antenna array. Let us assume that the incident direction is on the yoz plane. The number of slot vibrators along the x-axis over a length of  $2l$  is  $M$ , the distance between slots is  $\Delta x$ , the slot width is

W, the number of vibrators long the y-axis is N and the spacing is  $\Delta y$ . The contribution of the entire antenna array to the RCS is the phase sum of two terms, i.e., the mode term and structure term.<sup>4</sup>

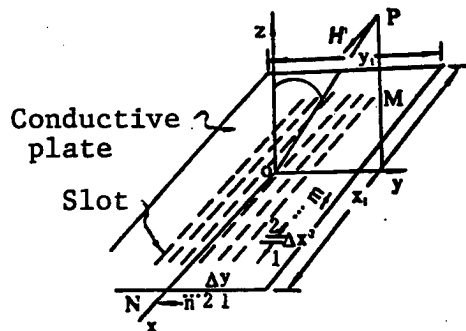


Figure 1. Array Antenna

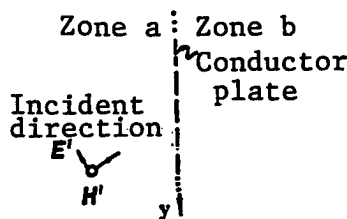


Figure 2. Side View of Array

### 1. Computation of Mode Term

The plate can be considered infinite. Its conductive wall divides the space into zones a and b. Using the equivalence theorem [See Reference 5, Sec. 3-5], the problem can be split into two, as shown in Figure 3. When the aperture is blocked by the conductive plate and replaced with an equivalent magnetic flux  $M_1$  [ $I = (m-1)N + n$ ,  $m = 1, 2, \dots, M$ ,  $n = 1, 2, \dots, N$ ], the field in zone a remains unchanged. When the aperture is blocked by the conductive plate and replaced by an equivalent magnetic flux  $-M_1$ , the field in zone b remains constant as well. [passage omitted]

### III. Results and Analysis

As an example, computation was done on a  $4 \times 8$  half-wavelength slot-array antenna with  $\lambda = 3.2$  cm. The slot width is  $W = 0.0125\lambda$ . The end-point spacing in the x direction is a half-wavelength and the slot spacing in the y direction is also a half-wavelength. The plate size is  $4.0625\lambda \times 10\lambda$ . Figure 4 shows the RCS of the antenna as a function of observation angle  $\theta$ . The unit of RCS in the figure is  $\text{dBA}^2$ . From the figure one can see that the mode-scattering term generated by the excitation of the incident wave at the slot is far less than the structure term when the mutual coupling between slots is taken into consideration. For instance, it is 21.340 dB less at

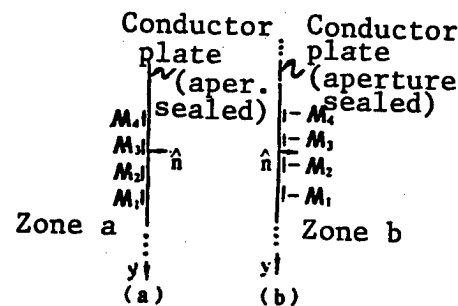


Figure 3. Equivalent Zones

the axial direction. Hence, the resultant far scattering field essentially varies according to the pattern of the plate structure term in the range of  $0-60^\circ$ . Therefore, it is quantitatively demonstrated that structural scattering from the plate is the dominating term in the mechanism of a slot-array antenna. In order to effectively reduce the RCS of a slot-array antenna, it is necessary to minimize the contribution of the plate. For example, a traveling wave slot-array antenna (non-resonant) may be used to offset the peak of its emission from its peak direction of scattering to lower the RCS at the nose of the aircraft. In addition, a conformal curved surface, such as a cylindrical, conical, spherical, ellipsoidal or paraboloidal surface, can be used instead of a flat plate to significantly reduce the contribution of the structure term to the RCS.<sup>8</sup>

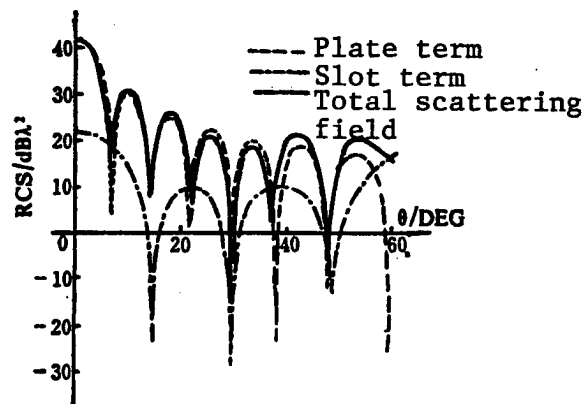


Figure 4. RCS of Planar Slot-Array Antenna vs. Observation Angle

An experimental antenna was made based on the parameters of the model used in the computation. The RCS was measured with an outdoor quasi-monostatic RCS measurement system (see Figure 5). The measured result is compared to the theoretical value, and they are found to be in good agreement. The rotation angle  $\alpha$  corresponding to the maximum RCS value in Figure 5 should correspond to  $\theta = 0^\circ$  in Figure 4.

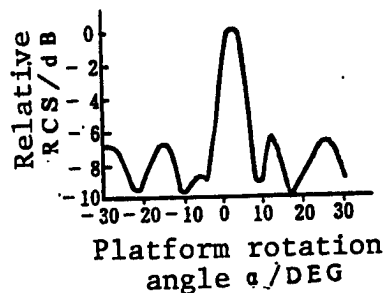


Figure 5. Measured RCS of Planar Slot-Array Antenna

#### IV. Conclusions

Theoretical analysis and numerical computation of the RCS of a planar slot-array antenna was carried out using the momentum method, physical optics method and singularity elimination technique. It was found that the structure term plays a dominant role in the scattering mechanism. Viable technical approaches of engineering value are presented to reduce RCS.

#### References

1. C. H. Liang and D. K. Cheng, "Electromagnetic Fields Coupled Into a Cavity With a Slot-Aperture Under Resonant Conditions," *IEEE TRANS.*, Vol AP-30, 1982, pp 664-672.
2. R. F. Harrington, "Resonant Behavior of a Small Aperture Backed by a Conducting Body," *IEEE TRANS.*, Vol AP-30, 1982, pp 205-212.
3. R. F. Harrington and D. T. Auckland, "Electromagnetic Transmission Through Narrow Slot in Thick Conducting Screens," *IEEE TRANS.*, Vol AP-28, 1980, pp 616-622.
4. Ruan Yingzheng, "Antenna Scattering Mechanism and Radar Cross Section Reduction," *YUHANG XUEBAO [JOURNAL OF THE CHINESE SOCIETY OF ASTRONAUTICS]*, No 4, 1990, pp 94-100 [translated in full in JPRS-CST-91-008, 3 Apr 91 pp 1-5].
5. R. F. Harrington, "Time-Harmonic Electromagnetic Fields," 1961, McGraw Hill, New York.
6. Deng Shuhui and Wang Dinghua [3769 1353 5478], "Planar Antennas," *DIANZI KEJI DAXUE XUEBAO [JOURNAL OF THE UNIVERSITY OF ELECTRONIC SCIENCE AND TECHNOLOGY (UEST) OF CHINA]*, Vol 19, No 2, 1990, pp 165-169.
7. W. L. Stutzman and G. A. Thiele, "Antenna Theory and Design," 1981, Wiley, New York, p 455.
8. Deng Shuhui and Ruan Yingzheng, "Electromagnetic Scattering from a Reflective Surface and Shape Optimization," *YUHANG XUEBAO [JOURNAL OF THE CHINESE SOCIETY OF ASTRONAUTICS]* (to be published).

#### Deng Shuhui

Born in 1963, he graduated in 1985 from the Radio Department of Lanzhou University. In 1988 and 1991, he earned his Master's and Ph.D. from the Departments of Electromagnetic Field Engineering and Microwave Engineering, respectively, at UEST. Presently, he is involved in teaching and research in microwave engineering. His primary research interest is in target electromagnetic scattering, and antenna and electromagnetic field theory. He has published 16 papers in technical journals worldwide.

#### Ruan Yingzheng

Born in 1939, he graduated from Chengdu Institute of Radio Engineering in 1960. Between 1982 and 1985, he furthered his study at New York Polytechnic University. Presently, he is engaged in teaching and research in the field of antennas, electromagnetic theory and target characteristics. He has authored books such as "Radar Scattering Cross Section," "Fundamental Electromagnetic Radiation Theory," and "Theory and Application of Complex Projection," and has published more than 50 papers in technical journals worldwide. He has 10 certified research accomplishments and received four provincial technical progress awards. Presently, he is Chairman, Professor and Doctoral Advisor in the Department of Microwave Engineering at Chengdu UEST.

#### Study of Backscattering of Electromagnetic Missiles

92FE0801D Beijing DIANZI XUEBAO  
[ACTA ELECTRONICA SINICA] in Chinese  
Vol 20 No 6, Jun 92 pp 28-35

[Article by Wen Geyi [2429 5308 0001], Ruan Chengli [7086 2052 4409], and Lin Weigan [2651 3624 1626] of the Institute of Applied Physics, UEST, Chengdu, 610054: "Study of Backscattering of Electromagnetic Missiles"; MS received Feb 91, revised Jul 91 (cf. JPRS-CST-92-013, 29 Jun 92 pp 43-44)]

#### [Excerpts] Abstract

The backscattering of an electromagnetic missile with its energy decaying as  $r^{-\epsilon}$  by an ideal metallic elliptical cylinder and a sphere is described. The study shows that the rates of energy decay for the backscattered fields from the elliptical cylinder and sphere are proportional to  $r^{-(1+\epsilon)}$  and  $r^{-(2+\epsilon)}$ , respectively.

Key Words: electromagnetic missile, backscattering, backscattered field.

#### I. Introduction

The concept of an electromagnetic missile was first presented by T. T. Wu in 1985. It is a transient electromagnetic wave of finite energy that does not decay according to  $r^{-2}$  as a conventional spherical wave in the far field. Instead, it decays slowly at an arbitrary rate.

This excellent slow decay characteristic of the electromagnetic missile can be used to increase the effective range and improve the performance of radars.<sup>1</sup> Properties such as short duration (picoseconds) and high peak power (giga-watts) can also be used to enhance the detection capability of the radar for low-RCS or stealth targets. Therefore, there is a need to have a profound understanding of the generation and propagation of electromagnetic missiles from both theoretical and practical viewpoints.

In the past few years, a great deal of theoretical and experimental work has been done on electromagnetic missiles. Several electromagnetic missile launchers were constructed. This demonstrated that it is not that difficult to make electromagnetic missiles a reality. Besides constructing a variety of electromagnetic missile launchers, there is another research topic of considerable significance, i.e., the study of scattering characteristics of electromagnetic missiles from different target shapes.

It is well known that the energy of a conventional electromagnetic wave decays according to  $r^{-1}$  in two-dimensional space. Hence, the energy of scattered field decays as a function of  $r^{-2}$ . In three-dimensional space, the energy of a conventional electromagnetic field decays as a function of  $r^{-2}$  and that of the corresponding scattered field decays according to  $r^{-4}$ . Recently, Myers and T. T. Wu have studied the backscattering of electromagnetic missiles from a plate. The results show that the energy of the backscattered field of an electromagnetic missile decaying as a function of  $r^{-\epsilon}$  from a flat plate still decays according to  $r^{-\epsilon}$  ( $0 < \epsilon < 1$ ). This is much slower than the decay of the energy of a conventional scattered field.

This study involves the backscattering of electromagnetic missiles from ideal elliptical cylindrical and spherical conductors of infinite length. The results indicate that the backscattered fields of the elliptical cylinder and sphere decay according to  $r^{-(1+\epsilon)}$  and  $r^{-(2+\epsilon)}$ , respectively. They are considerably faster than the decay of the backscattered field from a flat plate. However, they are slower than the decays of conventional two- and three-dimensional scattered fields, which are proportional to  $r^{-2}$  and  $r^{-4}$ , respectively. [passage omitted]

#### IV. Conclusions

This paper describes the backscattering of an electromagnetic missile decaying as a function of  $r^{-\epsilon}$  from an elliptical cylinder conductor and a sphere conductor. An analysis shows that their scattered fields are proportional to  $r^{-(1+\epsilon)}$  and  $r^{-(2+\epsilon)}$ , respectively. This conclusion is an important reference point in counter-stealth technology. As far as counter-stealth is concerned, an electromagnetic missile is an excellent electromagnetic pulse. When used in impulse radars, it can effectively counter the effects of [radar] absorbent materials (RAM) and profile stealth technology. The signal-to-noise ratio of the radar can be improved and the effectiveness of the radar can

be enhanced. It is of great significance to further investigate the theory and practice of backscattering of electromagnetic missiles from other targets. There is a great deal of work still to be done in this field.

#### References

1. J. M. Myers and T. T. Wu, PROC. SPIE, Vol 1226, 1990, pp 29-31.
2. T. T. Wu, JOUR. APPL. PHYS., Vol 57, No 7, 1985, pp 2370-2373.
3. H. M. Shen and T. T. Wu, JOUR. APPL. PHYS., Vol 66, No 19, 1989, pp 4025-4034.
4. D. S. Jones, "The Theory of Electromagnetism," Pergamon Press, 1964.
5. J. A. Stratton, "Electromagnetic Theory," McGraw Hill Book Co., 1941.

#### Wen Geyi, Associate Professor from Pingjiang, Hunan

Graduated from Xidian University in 1982 and earned his Master's and Ph.D. degrees from the same university in 1984 and 1987, respectively. He conducted his first phase of post-doctoral research at Southeast University in 1988-1990 and began the second phase of post-doctoral work at Chengdu UEST in 1991. In recent years, his research has been in theoretical and applied electromagnetic fields and microwave technology. Dr. Wen is an editor of the IEEE TRANS. on MTT and has published over 30 papers in technical journals worldwide.

#### Ruan Chengli, Professor from Hongan, Hubei

Graduated from Chengdu UEST in 1967 and earned his Master's and Ph.D. degrees in engineering from the same institution in 1981 and 1984, respectively. His primary areas of interest are theory and applications of slowly decaying electromagnetic waves, theory of electromagnetic scattering and target characteristics, microwave theory, and microwave measurement and millimeter-wave technology. He received a second-class theoretical achievement from the Ministry of Machine-Building and Electronics Industry (MMEI) in 1988, a third-class national science and technology progress award in 1989, another second-class theoretical achievement from MMEI in 1990 and a national significant contributor award for Ph.D. in 1991.

#### Lin Weigan, Professor and Academic Committee Member of the Chinese Academy of Sciences

Graduated from National Qinghua University (Kunming) in 1939 and earned his Master's and Ph.D. degrees from the University of California at Berkeley in 1947 and 1950, respectively. He returned to China as a professor in 1951. In 1990, he was chosen as a Fellow of the School of Electromagnetism at Massachusetts Institute of Technology. Since September 1984, he has been Chairman of the Microwave Committee of the Chinese Society of Electronics. Since September 1986, he has been the Chairman of the Chinese chapter of IEEE-MTT. He is on the editorial board of DIANZI XUEBAO [ACTA ELECTRONICA SINICA]. He has published over 100 papers and received more than 20 national awards. He is an internationally renowned microwave expert.